JOURNAL OF GEOPHYSICAL RESEARCH, VOL. 100, NO. D1, PAGES 1167–1197, JANUARY 20, 1995

Calculation of surface and top of atmosphere radiative fluxes from physical quantities based on ISCCP data sets 2. Validation and first results

W. B. Rossow

NASA Goddard Institute for Space Studies, New York

Y.-C. Zhang

Department of Applied Physics, Columbia University, New York

Abstract. We use global, multiyear observations of the properties of clouds, the atmosphere, and the surface to calculate global shortwave (SW) and longwave (LW) fluxes at the top of the atmosphere and at the surface at a resolution of 280 km and 3 hours for every third month from April 1985 to January 1989. Our validation studies suggest that the specification of cloud effects is no longer the dominant uncertainty in reconstructing the radiative fluxes at the top of atmosphere and at the surface. Rather cloud property uncertainties are now roughly equal contributors to the flux uncertainty, along with surface and atmospheric properties. Overall, the estimated uncertainties in regional, monthly mean fluxes, based on comparisons to more direct measurements, are as follows: for $S\uparrow_t$, 11 W/m² bias with a rms scatter of 7 W/m² (the bias may be as little as 5 W/m²); for $L\uparrow_t$, -1 W/m² bias with a rms scatter of 4 W/m²; for $S\downarrow_s$, 10 – 20 W/m² bias with a rms scatter of 10 – 15 W/m² (the bias may only be ≈ 10 W/m² caused by aerosols); for $S\uparrow_s$, ≈ 3 W/m² bias with a rms scatter of 10 W/m²; for $L\downarrow_s$, probably < 15 W/m² bias (but with variable sign) with a rms scatter of 15 W/m² (bias and scatter depend most on atmospheric temperature uncertainties); and for $L\uparrow_s$, ≲ 12 W/m² and ≲ 24 W/m² for combined bias and scatter over oceans and land, respectively (very sensitive to surface temperature determinations). The resulting SW and LW flux data sets suggest the following conclusions: (1) The net SW heating of Earth appears predominantly at the surface, whereas the net LW cooling arises predominantly from the atmosphere. The net cooling effect of clouds on top of atmospheric radiation appears primarily at the surface rather than in the atmosphere. (2) Clouds have almost no net effect on the global mean radiation balance of the atmosphere, but they enhance the latitudinal gradient in the LW cooling and reinforce the radiative forcing for the mean atmospheric circulation. Clouds act to mute seasonal contrasts however. (3) Clouds enhance the land-ocean contrasts of the atmospheric cooling, reinforcing the growth of standing eddy motions; but reduce land-ocean contrasts of the surface heating.

1. Introduction

The earliest studies of the radiation balance at the top of the atmosphere [e.g., *Simpson,* 1929; *Brooks,* 1949] calculated the shortwave (SW) and longwave (LW) flux components of the balance from estimates of the properties of the atmosphere, clouds, and surface because no direct flux measurements were available. Budyko [see *Budyko,* 1974, and references therein] used the same approach to infer the energy budget at the surface. The advent of satellite measurements of radiation in the 1960s led to more direct estimates of the top of atmosphere (TOA) fluxes [e.g., *Vonder Haar and Suomi,* 1971; *Raschke et al.,* 1973], an approach that continues in use today with refined analysis techniques and better accuracy satellite measurements [e.g., *Kyle et al.,* 1990, 1993; *Harrison et al.,* 1990; *Ardanuy et al.,* 1991]. Since satellites do not measure surface radiation directly, models are used to link satellite observations and surface radiation [e.g., *Gautier et al.,* 1980; *Stuhlmann et al.,* 1990; *Bishop and Rossow,* 1991; *Darnell et al.,* 1992; *Pinker and Laszlo,* 1992; *Li et al.,* 1993].

Paper number 94JD02746.
0148-0227/95/94JD-02746$05.00

The advent of more accurate global observations of cloud, atmosphere, and surface properties from satellites makes the earlier calculation technique attractive again because this approach naturally separates the effects of clouds on the radiation balance from other atmospheric and surface factors and allows for an explicit determination of the variations of radiative fluxes caused by each cloud property. Moreover, the radiative model and data sets used for these calculations can determine the cloud effects on both the TOA and the surface radiation balance in a self-consistent manner that allows for separation of the total planetary radiation balance into its atmospheric and surface components [*Rossow and Lacis,* 1990].

The International Satellite Cloud Climatology Project (ISCCP) cloud data sets [*Rossow and Schiffer,* 1991], when supplemented by some additional information (section 2.1), describe the variations of the key physical attributes of the clouds, atmosphere, and surface that affect the radiation balance. We use these data sets and a radiative transfer model from the Goddard Institute for Space Studies (GISS) general circulation model (GCM) (section 2.2) to calculate all of the individual radiative flux components shown in Table 1. In a companion paper [*Zhang et al.,* this issue] we describe the radiative transfer model and data inputs in detail, summarize comparisons of the model to more detailed radiation models, and evaluate the sensitivity of the calculated fluxes to uncertainties in the input physical quantities.

Table 1. Definitions of Symbols Representing Shortwave and Longwave Radiative Fluxes, Net Radiative Fluxes, and Other Combinations of the Radiative Fluxes

Symbols	Definition
$S\downarrow_t$, $S\downarrow_s$	downward shortwave flux at top of atmosphere and surface, where $S\downarrow_t = \mu_0 S_0$
$S\uparrow_t$, $S\uparrow_s$	upward shortwave flux at top of atmosphere and surface
NS_t	net shortwave flux into top of atmosphere = $S\downarrow_t - S\uparrow_t$
NS_s	net shortwave flux into surface = $S\downarrow_s - S\uparrow_s$
NS_a	net shortwave flux into atmosphere = $NS_t - NS_s$
Alb_t, Alb_s	= $S\uparrow_t/S\downarrow_t$, $S\uparrow_s/S\downarrow_s$
SW Trans	= $S\downarrow_t/S\downarrow_s$
$L\downarrow_t$, $L\downarrow_s$	downward longwave flux at top of atmosphere and surface, where $L\downarrow_t = 0$
$L\uparrow_t$, $L\uparrow_s$	upward longwave flux at top of atmosphere and surface
NL_t	net longwave flux into top of atmosphere = $-L\uparrow_t$
NL_s	net longwave flux into surface = $L\downarrow_s - L\uparrow_s$
NL_a	net longwave flux into atmosphere = $NL_t - NL_s$
LW Trans	= $L\uparrow_t/L\uparrow_s$
Emiss	= $L\downarrow_s/L\uparrow_s$
N_t	total net flux into top of atmosphere = $NS_t + NL_t$
N_s	total net flux into surface = $NS_s + NL_s$
N_a	total net flux into atmosphere = $N_t - N_s$
CLR-X	value with no cloud cover, e.g., CLR-$S\uparrow_t$ is the upward shortwave flux at the top of atmosphere with 0% cloud
CLD-X	value with 100% cloud cover, e.g., CLD-$S\uparrow_t$ is the upward shortwave flux at the top of atmosphere with 100% cloud
CFC-X	difference between full sky flux and clear sky value, (F – CLR-F), e.g., CFC-$S\uparrow_t$ is the difference between the upward shortwave flux at the top of the atmosphere in a cloudy atmosphere and in the same atmosphere with no clouds

Albedo refers to radiation reflected from the surface or the surface and atmosphere, together. SW trans refers to the net transmission of SW downward through the atmosphere, including the effects of multiple scattering. LW trans is like an effective transmission of the surface-emitted LW through the atmosphere, but in fact most of the radiation from the surface is absorbed and reemitted and additional energy is transferred from the surface by latent and sensible heat exchanges. Likewise Emiss is like the effective amount of surface radiation that is reemitted downward from the atmosphere, but in fact a substantial fraction of the energy is transferred from the surface to the atmosphere by latent and sensible heat exchanges.

The focus of most radiation budget studies has been on determining the large-scale average net fluxes that affect the thermodynamic state of the climate system. However, studies of top of atmosphere flux balances and variations are not sufficient to determine the effects of clouds on the atmospheric and oceanic circulations because these effects depend on the temporal, vertical, and horizontal distribution of the radiative energy *within* the atmosphere and ocean [*Webster and Stephens,* 1984]. The unprecedented spatial and temporal resolution of the ISCCP data sets creates the opportunity to describe the physical variations of the atmosphere (including clouds), together with the variations of the radiative fluxes, on the predominant time and space scales in the atmospheric general circulation. If we can do this with sufficient accuracy, then we may be able to learn the workings of the processes that link radiation with atmospheric motions: key feedbacks on this link are cloud processes which redistribute the radiative heating/cooling of the atmosphere as well as contribute additional latent heating by producing precipitation. Therefore we need to verify the flux calculations in much more detail than usual.

Our first flux data set provides complete global coverage at a spatial resolution of about 280 km every three hours for every third month from April 1985 to January 1989. The combination of fluxes and input physical variables is called FC data. In this paper we assess the fidelity of the results by comparing our calculated fluxes in section 3 with direct measurements by satellites and surface-based radiometers (data sets described in section 2.4). We conclude that there remain some problems that require more work; nevertheless, the uncertainties are small enough for a preliminary diagnosis of cloud radiative effects. Our first results are examined in section 4 to determine the average (global and annual) effects of clouds on the mean radiation balance at the top of the atmosphere and at the surface. We also examine how clouds alter the horizontal gradients and seasonal variations of the TOA and surface radiative balances. The unique feature of our analysis is that with self-consistent TOA and surface radiative fluxes, we can isolate the net radiative balance in the atmosphere, considered as a single layer, and determine the primary cloud radiative effects on the atmospheric circulation.

2. Data Sets and Analysis Method

2.1. Input Data

The primary input data sets to the radiative transfer model are the ISCCP C1 and C2 data sets [*Rossow and Schiffer,* 1991; *Rossow et al.,* 1991] for every third month from 1985 to January 1989 (also February and March 1990). ISCCP global data are produced by merging the analyses of narrowband (visible ≈ 0.6 μm and infrared ≈ 11 μm) radiances from the network of weather satellites with the TIROS operational vertical sounder (TOVS) daily analysis product produced by National Oceanic and Atmospheric Administration (NOAA) [*Smith et al.,* 1979; *McMillin,* 1991] and the weekly snow/ice cover data from NOAA/National Environmental Satellite Data and Information Service (NESDIS) and NAVY/NOAA Joint Ice Center [*Rossow et al.,* 1991]. ISCCP C1 data are global, three hourly data with a spatial resolution equivalent to 2.5° × 2.5° at the equator (about 280 km). The specific C1 parameters used for the

flux calculation are (1) column ozone abundance (O_3), atmospheric temperature profile (T_a), and humidity profile (reported as precipitable water amount, PW) from the surface to the lower stratosphere from TOVS (TOVS measures humidities only up to the 300 mbar level; humidities above this level are specified by the U.S. Standard Atmosphere [1976]); (2) surface temperature (T_s) and visible reflectance (R_s) from the ISCCP clear-sky composite; and (3) area-mean cloud parameters assigned to a single cloud layer: fractional cover (Cf), visible optical thickness (τ), and cloud top temperature (T_c). ISCCP C2 data are monthly averages of the C1 data which are used when C1 parameters are occasionally unavailable. The filling procedure also interpolates the more complete daytime cloud information into nighttime so that the input data set is globally and diurnally complete [*Zhang et al.*, 1994]. Some flux calculations are performed for individual satellite pixels (called CX data), representing areas about 4-7 km across and sampled at intervals of about 30 km every three hours; for cloudy pixels we use the retrieved values of τ and T_c with Cf = 100%.

Supplementary data sets used are (1) a climatology of cloud layer thicknesses as a function of cloud top height, latitude, and season based on rawinsonde and surface observations [*Poore et al.*, 1995]; (2) climatological aerosol optical thicknesses and compositions for the anthropogenic sulfate component are based on *Charlson et al.* [1991] and on *Toon and Pollack* [1976] for the natural background components; (3) latitude and month-dependent ozone profiles from *London et al.* [1976]; (4) global vegetation distribution and properties [*Matthews*, 1983]; and (5) a climatology of upper (< 5 mbar) stratospheric temperatures from *McClatchey* [1972].

2.2. Radiative Transfer Model

The model used in these calculations is from the GISS GCM [*Hansen et al.*, 1983] with some modifications to use the available data inputs better [*Zhang et al.*, this issue]. The model treats nongrey gaseous absorptions and thermal emission in a vertically inhomogeneous, multiple-scattering atmosphere [*Lacis and Oinas*, 1991] and calculates the spectral variation of the upwelling and downwelling SW (0.2 – 5.0 μm) and LW (5.0 – 200.0 μm) fluxes at the edges of each atmospheric layer from the top of the atmosphere (TOA = 100 km) to the surface. All radiatively significant atmospheric constituents are included (H_2O, CO_2, O_3, O_2, NO_2, N_2O, CH_4, CCl_3F, CCl_2F_3); abundances of the well-mixed trace gases are set to their 1980 values [*Hansen et al.*, 1988]. The vertical distribution of O_3 is specified from *London et al.* [1976] with the total column abundance adjusted to match regional, daily values from the NOAA TOVS data set. The vertical distribution and abundance of H_2O up to the 300 mbar level are specified daily at each location from the NOAA TOVS data set; values above the 300 mbar are specified by the *U.S. Standard Atmosphere* (1976). LW continuum absorption by water vapor incorporates the self and foreign broadening contributions formulated by *Roberts et al.* [1976].

Realistic spectral variations of cloud (composed of liquid water spheres with an effective radius of 10 μm and a size distribution variance of 0.1) and aerosol optical properties are determined for the model from off-line, complete Mie scattering computations [*Hansen and Travis*, 1974] and used in a "single Gauss point" method to treat the direct and diffuse components of scattered radiation. The spectrally varying values of cloud optical thickness (τ) are referenced to the visible (0.6 μm wavelength) value (henceforth all quoted values of optical thickness are for this wavelength unless stated otherwise). The amounts and optical properties of five types of aerosols (global stratosphere, continental troposphere, oceanic troposphere, desert troposphere, and haze) are specified climatologically; each type is a specified mixture of 11 kinds of aerosols, including silicates, sulfates, and carbon soot [*Hansen et al.*, 1983]. The solar constant, S_0, is 1367 W/m² [*Hickey et al.*, 1988]; the insolation at TOA ($S\downarrow_t$) at a particular location and time (precise to 1 min) is calculated as a function of the Sun-Earth distance for each day of the year and the solar zenith angle. The values of cosine of the solar zenith angle (μ_0) used in the calculations are averaged over the 3-hour interval centered on the nominal times UTC of each ISCCP C1 data set.

The cloud-free atmosphere is divided into eleven fixed pressure layers, defined by pressures of 1000 (or surface pressure, P_s), 800, 680, 560, 440, 310, 180, 70, 30, 5, 2, and 0 mbar (the actual number of tropospheric layers varies with the topography and tropopause height). The temperature of the two layers above the 5 mbar level are specified as a function of month and latitude from climatology [*McClatchey et al.*, 1972], while the temperatures of all other layers are specified daily at each location by the NOAA TOVS data set. For each ISCCP equal-area map grid cell at 3-hour intervals, clouds are represented by a single layer (which may be more than one model layer thick) inserted as defined by the cloud top pressure (P_c) and a cloud base pressure (P_b). The value of P_c is found from T_c by interpolation on the TOVS atmospheric temperature profile. The value of P_b is determined by adding climatological cloud layer thicknesses as a pressure increment to P_c [*Poore et al.*, 1995]. A minimum clear layer thickness at the surface is also specified from the same climatology, unless it requires a cloud layer thickness less than the climatological minimum, in which case $P_b = P_s$.

The surface in each ISCCP map grid cell is treated as a area-weighted mixture of up to four different surface types: land, land ice, ocean, and sea ice. Land is further subdivided into eight types: desert, tundra, grassland, grassland with shrubs, grassland with some trees, deciduous forest, evergreen forest, and rainforest [*Matthews*, 1983]. Land can be covered with snow as specified by the NOAA snow cover data set. Land albedos (given as values from 0.0 to 1.0) are assumed to be Lambertian but actually vary with monthly mean solar zenith angle because they are determined from ISCCP retrievals of surface visible reflectance, R_s. The ocean directional albedo is specified as a function of solar zenith angle and wind speed (fixed at 2 m s^{-1} in these calculations) by an empirical model tuned to match the ISCCP values of R_s. Land and ice surface albedos are specified in two spectral parts covering the broadband "visible" (≈ 0.2 – 0.7 μm) and broadband near-IR (≈ 0.7 – 5.0 μm). The visible directional albedo is equal to the ISCCP value of R_s and the near-IR albedo is obtained from R_s by multiplying by a spectral ratio for each surface type (with seasonal variations). All snow cover is treated as pure fresh snow to determine the spectral ratio.

Surface "skin" temperatures are specified at each location and time from the ISCCP values (T_s) that are retrieved from narrowband (≈ 11 μm wavelength) radiances assuming unit emissivity for all surfaces. The same assumption is used in the calculation of total LW fluxes. The radiative model allows for near-surface air temperatures that are different from the surface skin temperatures: the near-surface air temperature is determined by extrapolating the TOVS atmospheric temperature profile to the surface pressure.

2.3. Output Quantities

With all of the input parameters obtained from the ISCCP data sets or specified from climatologies, the radiative transfer model calculates complete vertical profiles of all flux components (Table 1), both SW and LW, for each equal-area map cell over the whole globe, every three hours over each month. Because each cloud is treated as a single layer, we focus our attention on the fluxes at

TOA (100 km) and the surface that are less sensitive to cloud vertical structure. The output data set contains the parameters in Table 1 for full sky (actual cloud cover), completely overcast sky (indicated by CLD), and clear sky (CLR) as well as all the input C1/C2 parameters (including interpolated values). All fluxes are positive quantities with their direction indicated by arrow symbols; all net fluxes are defined so that positive (negative) values indicate heating (cooling). Some additional combinations of these fluxes are also defined in Table 1. This combined data set is referred to as the FC data set, which we have produced for every third month from April 1985 to January 1989. Fluxes calculated for individual satellite pixels are called FCX data.

2.4. Validation Data Sets

The TOA fluxes are compared in section 3.1 to coincident results from the Earth Radiation Budget Experiment (ERBE) [*Ramanathan et al.*, 1989; *Harrison et al.*, 1990] produced by a combination of measurements from the narrow-field-of-view scanners on the ERBS and at least one NOAA polar orbiting satellite (NOAA 9 observations are used for April 1985 through December 1986, NOAA 10 observations are used from April 1987 to January 1989, and both NOAA 9 and NOAA 10 are used for January 1987). The ERBE S4 data set reports daily mean, monthly mean-hourly (averages at each hour over the month) and monthly mean values of $S\uparrow_t$ (0.2 – 5.0 μm), planetary albedo (= $S\uparrow_t/S\downarrow_t$) and $L\uparrow_t$ (5.0 – 50.0 μm) for full-sky, and clear-sky conditions in an equal-angle map grid with 2.5° resolution. Full sky refers to averages of all direct observations, whereas clear sky refers to average values collected under clear conditions as determined by the ERBE scene identification procedure [*Wielicki and Green*, 1989]. Both the daily mean and the monthly mean-hourly results are constructed from 1 month of observations at 4 varying times of day (for two satellites) [*Brooks et al.*, 1986].

The calculated surface fluxes are compared in section 3.2 to coincident values from the Global Energy Balance Archive (GEBA) data set. GEBA is a climatology of monthly mean surface energy fluxes, including radiative, that is constructed from direct measurements supplemented by satellite analyses and bulk transfer formulas, especially over oceans [*Ohmura and Gilgen*, 1991]. We compare directly measured monthly mean values of $S\downarrow_s$ and $L\downarrow_s$.

We also compare calculated surface fluxes to four sets of detailed surface measurements of $S\downarrow_s$ and $L\downarrow_s$ at high time resolution. The first data set was collected during the first cirrus cloud experiment of the First ISCCP Regional Experiment (FIRE) to provide test data for development of methods to infer surface radiative fluxes from satellite observations [*Whitlock et al.*, 1990a, b, c]. This collection reports values of $S\downarrow_s$ from 17 stations and $L\downarrow_s$ from 5 stations, all located in Wisconsin, with 1-minute time resolution over the period October 12 to November 2, 1986. Two other data sets were collected from stations located in Barrow (Alaska) and at the south pole for October 1986. The fourth data set comes from ship measurements collected during the the Tropical Ocean-Global Atmosphere program – Coupled Ocean-Atmosphere Response Experiment (TOGA-COARE) pilot cruise from February 16 to March 10, 1990 [*Young et al.*, 1992]. Hourly mean values of $S\downarrow_s$, $L\downarrow_s$, and $L\uparrow_s$ are reported, together with many other parameters describing the conditions of the ocean surface water and surface meteorology [*Young et al.*, 1992].

Finally, we compare our calculated global values of $S\downarrow_s$ at the surface to four other global analyses of the same satellite radiance data by *Bishop and Rossow* [1991], *Stuhlmann et al.* [1990], and two from the first version of the international Surface Radiation Budget (SRB) project. The latter results are based on methods by *Pinker and Laszlo* [1992] and *Darnell et al.* [1992]. The *Bishop and Rossow,* results are daily mean values, while all others are monthly means.

3. Comparisons to Other Flux Measurements

The final assessment of the uncertainties in our calculated fluxes (henceforth, FC data) is made by comparison to more direct measurements of the same quantities; however, none of these measurements directly represents what is calculated. In particular, none of these measurements matches the space-time sampling of the values we obtain from the ISCCP data set, so that some care must be exercised to explore the effects of different sampling on the comparisons. Because overall agreement between two sets of averaged quantities may hide important systematic differences, we emphasize comparisons over more than one space-time scale, where possible, and examine differences as functions of the physical quantities used in the calculations.

3.1. ERBE Flux Measurements

To obtain values of the TOA SW and LW fluxes, the direct broadband radiance measurements from the ERBE satellites (and from its predecessor missions) must be altered in three ways [*House et al.*, 1986; *Smith et al.*, 1986]. (1) Corrections are made to account for the fact that the sensitivity of the instruments is not the same at all wavelengths in the SW (0.2 – 5.0 μm) and LW (5.0 – 50.0 μm); this correction includes the radiometric calibration as well. Note that as much as 2% of the LW energy is emitted at wavelengths beyond 50.0 μm and must be accounted for in the calibration. (2) Some model [*Suttles et al.*, 1988, 1989] of the angular variation of the *radiances* is needed to convert them to *fluxes* at the top of the atmosphere (note that different analyses have used different locations for the top of the atmosphere, which for ERBE is 30 km, cf. *Kyle et al.* [1990]). The angle models, in turn, depend on the type of surface and the amount of cloud present in the observed scene, so some procedure [*Wielicki and Green*, 1989] is required to identify different scene types. (3) Some procedure is needed to obtain proper averages of the fluxes from temporally and spatially sparse samples [*Brooks et al.*, 1986]. A long series of satellite Earth Radiation Budget experiments [*House et al.*, 1986] has culminated in the ERBE mission with progressive improvements of methodologies in all three areas.

In the ERBE time/space averaging subsystem, directional albedo models for nine scene types define the change of scene albedo with solar zenith angle over the diurnal cycle. A "half-sine" model is used to interpolate LW flux over the diurnal cycle [cf. *Brooks and Minnis*, 1984a]. These two models are used to calculate $S\uparrow_t$ (given $S\downarrow_t$ and scene albedo) and $L\uparrow_t$ at 24 local hours (on the half hour) for days that have at least one radiance measurement. Daily averages are constructed from the 24 values on those days with at least one measurement. Two monthly mean values are then obtained, one by averaging over the month at each hour of the day (monthly mean-hourly), using only days with actual observations, and one by averaging over the daily mean values (monthly mean), using interpolated daily averages for LW. Various estimates of the uncertainties in regional (i.e., single 2.5° map grid cells) monthly mean fluxes associated with using these diurnal models suggest values from 3 – 7 W/m², ranging up to 10 – 20 W/m² in some locations, for the combined results from two satellites [*Brooks and Minnis*, 1984b, *Harrison et al.*, 1990; *Rieland and Raschke*, 1991; *Hartmann et al.*, 1991]. These estimates do not include the effect

of missing observations during the month. *Hartmann et al.* [1991] show that the magnitude of the spurious semidiurnal variation produced by ERBE sampling is further reduced by averaging over several years of data. Hence the 3 – 7 W/m² uncertainty estimate has to be taken as a lower limit for the effects of using diurnal models to compensate for sparse sampling.

The ERBE monthly mean flux values do not cover the whole globe and the geographic coverage varies from month to month, so when comparing our TOA fluxes with those from ERBE, we restrict the comparison to those map grid cells where ERBE reports monthly mean values. We also remap the ERBE values, originally in a 2.5° × 2.5° equal-angle map into our equal-area map (equivalent to 2.5° × 2.5° resolution at the equator). For comparisons of monthly values of $S\downarrow_t$ and total net (N_t) fluxes we use values derived directly from ERBE values of $S\uparrow_t$, albedo and $L\uparrow_t$ for consistency in spatial sampling. Note that errors in global mean fluxes associated with incomplete global coverage (estimated using the complete ISCCP values sampled to mimic ERBE sampling) are important when considering the global mean radiation balance: the global net balance from ERBE can be altered by up to 5 W/m² by incomplete coverage.

One estimate of the overall uncertainty in the ERBE values can be obtained by comparison to another set of values from the Nimbus 7 ERB experiment [*Kyle et al.*, 1990]. Table 2 compares global, annual mean values of planetary albedo ($S\uparrow_t/S\downarrow_t$), $L\uparrow_t$, and N_t from ERBE, Nimbus 7, some earlier results, and this work. Although the preferred values for Nimbus 7 and ERBE agree to within about 1 W/m², both results are out of balance by about +5 W/m² (about twice the estimated current greenhouse imbalance). Moreover, there are a variety of other published results, based on these same data sets, that differ by about ± 2 W/m² for LW and ± 5 W/m² for SW. *Harrison et al.* [1990] summarize various estimates of the uncertainties in ERBE results as suggesting biases of full-sky, regional monthly means ≤ 1 W/m² with rms uncertainties of 3 and 5 W/m² for LW and SW, respectively. On the other hand, *Stephens and Greenwald* [1991a] report that Nimbus 7 clear-sky SW fluxes are larger than ERBE values by about 3 W/m² and the clear-sky LW fluxes are smaller than ERBE by about 5 W/m². Moreover, regional (rms) differences in monthly mean fluxes between overlapping Nimbus 7 and ERBE data are of the order 10 – 15 W/m² [*Kyle et al.*, 1990].

For each map grid cell for each of 16 months in 1985 through 1988, we have compared our calculations (FC) to monthly mean ERBE values of $S\downarrow_t$, $S\uparrow_t$, albedo (= $S\uparrow_t/S\downarrow_t$), NS_t, $L\uparrow_t$, and N_t for both full sky and clear sky, respectively. Since there are no unusual results in any particular month, we summarize all the comparisons in Table 3 with average statistics over the four examples of each month (the FC values in this table are matched to the incomplete spatial coverage of ERBE). For all quantities except cloud flux change (CFC) (see Table 1 for definition), the average differences between monthly mean ISCCP and ERBE values for individual map grid cells are ≤ 10 W/m² with standard deviations < 13 W/m². The average differences for both full-sky and clear-sky albedos are < 0.035 with a maximum standard deviation of 0.04. The largest biases occur in $S\uparrow_t$ and CLR-$L\uparrow_t$; the largest rms differences are for CFC. When individual map grid cell values from ERBE (ordinate) and FC (abscissa) for each month are plotted against each other, all the linear correlation coefficients are ≥ 0.9. The normal deviations (rms distance of each point from the least squares linear fit) are < 8 W/m² for SW fluxes (< 0.03 for albedos) and about 4 W/m² for LW fluxes. More detailed results are described next, but we note that overall, the differences between ERBE and our calculated fluxes are not any larger than the estimated uncertainties in the ERBE values. This overview hides important details, however.

We illustrate the comparisons using results from July 1986 and January 1987 because they have the largest global coverage of any July and January in the ERBE results (limited by clear-sky albedo values), 91 and 94%, respectively. Since the monthly mean-hourly and monthly mean values are very close, we use the latter for comparisons; however, we also compare daily mean values and examine diurnal variations using the monthly mean-hourly values. All of the comparisons discussed below have been done for all 16 months of results.

Shortwave (SW) fluxes. Each FC value represents an average over a 3-hour interval, whereas each ERBE value is interpreted as an instantaneous value at the center of each hourly interval (the time of peak SW irradiance at local noon is not captured, instead values for 1130 and 1230 LT are reported). Because rapid variations of solar zenith angle with time of day produce very large SW flux variations, we have found that the best procedure for comparing diurnal variations from ERBE and FC (using monthly mean-hourly values at each location) is to calculate matching average values for each 3-hour interval from the hourly ERBE values. After converting each FC value from universal time convention (UTC) to local time (LT) for each longitude, we average four ERBE values around the

Table 2. Comparison of Annual, Global Mean Radiation Budgets at Top of Atmosphere

Source	NL_t	Alb_t	N_t
Ellis and Vonder Haar [1976]	-236	0.304	(1.9)
Jacobowitz et al. [1979]	-234	0.31	(1.8)
Ohring and Gruber [1983]	-244	0.31	(-8.2)
Nimbus 7 NFOV	-233	0.331	-4.70
Nimbus 7 WFOV – H	-229	0.31	6.46
Nimbus 7 WFOV – K	-234.88	0.2988	5.62 **
ERBE WFOV NF	-235.25	0.2825	9.67
ERBE WFOV SF	-234.11	0.2883	8.89
ERBE scanner	-234.50	0.2989	4.79 **
ERBE scanner (matched)	-235.2	0.291	7.9
FC (this work)	-234.24	0.3264	-4.11 **

The Earth Radiation Budget Experiment (ERBE) and Flux-Cloud data set (FC) (this work) averages are 4-month annual averages for 1985 – 1988. Units are watts per meter square (W/m²) except for albedo. Adopted from *Hartmann et al.* [1986] and *Kyle et al.* [1990], indicated by H and K, respectively. Entries for N_t in parentheses are calculated from the albedo values using a mean value of $S\downarrow_t$ = 341.75 W/m². Rows marked by asterisks indicate preferred values from each experiment. NFOV, narrow field-of-view; WFOV, wide field-of-view.

Table 3. Summary of Statistics From Comparison of Monthly Mean Maps of Top of Atmosphere Fluxes Obtained From ERBE and FC Data Sets With the Same Spatial Coverage as the ERBE Results and Shown as Global Averages Over Sixteen Months

Quantity	Global Average		Mean		Regression			Normal
	ERBE	FC	Difference	s.d.	Correlation	Slope	Intercept	Deviation
$S\downarrow_t$	351.7	351.9	0.26	2.04	1.000	0.996	0.96	1.28
$S\uparrow_t$	102.5	113.2	10.66	9.47	0.979	0.942	-4.06	6.53
Alb_t	0.291	0.322	0.033	0.032	0.969	0.938	-0.012	0.022
CLR-$S\uparrow_t$	53.7	57.8	4.07	11.02	0.949	1.027	-5.64	7.61
CLR-Alb_t	0.153	0.164	0.012	0.040	0.940	1.073	-0.025	0.027
NS_t	249.2	238.7	-10.54	9.28	0.996	1.014	7.31	6.42
CLR-NS_t	297.9	294.1	-3.89	11.27	0.994	1.008	1.37	7.84
$L\uparrow_t$	235.2	234.1	-1.09	7.37	0.984	1.128	-28.92	4.05
CLR-$L\uparrow_t$	266.7	257.5	-9.16	7.03	0.983	1.116	-20.71	3.94
N_t	13.9	4.6	-9.29	11.77	0.990	0.990	9.28	8.31
CLR-N_t	31.2	36.6	5.98	11.46	0.992	0.987	-5.30	7.93
CFC-SW_t	-48.8	-55.4	-6.91	11.93	0.938	0.930	2.96	8.48
CFC-LW_t	31.5	23.4	-7.69	7.69	0.920	1.223	2.97	4.44
CFC-N_t	-17.3	-32.0	-15.20	12.72	0.900	0.851	10.06	9.02

Each pair of values is the coordinates of points in a scatterplot with ERBE values on the ordinate and FC values on the abscissa. Regression statistics are from a linear least squares fit to the scatter of points. All values except slopes and albedos are in W/m².

FC center time (e.g., the ISCCP 1200 time, which represents an average from 1030 to 1330, is matched with an average of ERBE values from 1030, 1130, 1230, and 1330). Some of the disagreement occurs because we calculated SW fluxes at equally spaced intervals in time UTC, when more accurate results are obtained using equally spaced intervals in local time [*Zhang et al.*, this issue]. Note that other differences in temporal and spatial sampling produce significant discrepancies between ERBE and the full FC as illustrated by disagreements of up to 20 W/m² of the global averages of the monthly mean-hourly values of $S\downarrow_t$, which are defined solely by astronomy. This effect results primarily from month-to-month variations of time sampling in ERBE; averaging over the whole 16-month data set reduces the average difference of $S\downarrow_t$ to 0.26 W/m². To reduce these sampling effects further, we compare the mean diurnal variations of albedo instead of SW flux for both full sky and clear sky.

Figure 1 compares diurnal cycles of full-sky and clear-sky albedo from ERBE and FC averaged over all land and over all ocean areas for July 1986 (albedo values are averaged only over illuminated times and locations, so that values for local nighttime hours come from the summer polar regions). Presented this way, the variation of albedo over the day is associated with both changing solar zenith angle and changing geographic coverage. These figures generally show agreement to within about 0.04 for 0900, 1200, and 1500 where ERBE has more sampling. The clear albedos show excellent agreement (within 0.01 – 0.02) except over the polar regions (local nighttime in figure). Generally the FC sea ice albedos are higher than ERBE values by about 0.02, Greenland albedo is lower by 0.03 – 0.05, and Antarctic albedo (not shown in Figure 1) is lower by about 0.10. *Hartmann and Doelling* [1991] note overestimates by ERBE of clear-sky albedos over several snow covered land areas at high latitudes and over Greenland and Arctic sea ice [cf. *Stephens and Greenwald,* 1991a]. Total albedos (with clouds) from FC are slightly higher than ERBE values, consistent with an overall high bias of FC values of $S\uparrow_t$ relative to ERBE (Table 3); but FC total albedos are lower than ERBE in the polar regions (Figure 1).

The average shapes of the diurnal variations of $S\uparrow_t$ (which is controlled by solar zenith angle and geographic coverage variations) are nearly identical in both results, but the global comparisons in Figures 1, which average together regions with large and small diurnal variations of clouds, can hide some details. Figure 2 shows as examples the average diurnal variations of full-sky and clear-sky albedos for two regions with significant diurnal cloud variations: marine stratus clouds off the west coast of North America and the central United States in July 1986. The ERBE and FC results show the same small asymmetries of full-sky albedo about local noon: morning albedos are larger than afternoon values in the marine stratus regime [cf. *Minnis and Harrison,* 1984b], whereas afternoon albedos exceed morning values over the summertime continent because of convective activity. However, FC full-sky and clear-sky albedos are noticeably higher than ERBE values near dawn over the United States.

Figure 3 shows one example of the scatterplots of individual map grid values of daily mean $S\uparrow_t$ and CLR-$S\uparrow_t$ from the ERBE and FC results (we have examined such plots for 1 day from each of 16 months). Table 4 summarizes the statistics from such plots for July 15, 1986 and January 15, 1987. The correlation coefficients are ≥ 0.95. The mean differences are 11 and 4 W/m² and the standard deviations are 20 and 11 W/m², for full sky and clear sky, respectively. Removing the bias reduces the rms differences to about 15 W/m² for $S\uparrow_t$ and about 8 W/m² for CLR-$S\uparrow_t$.

Since reflected sunlight exhibits relatively large spatial and temporal variability [*Sèze and Rossow,* 1991a, b], differences in sampling between ERBE and ISCCP can introduce significant quasi-random differences in the two sets of measured fluxes. That the sampling effects causing scatter in Figure 3 are nearly random is illustrated in Table 5 by comparing daily and monthly mean values of $S\uparrow_t$ averaged to lower spatial resolution (10° × 10°). Note that the rms differences in $S\uparrow_t$ are reduced more by the spatial averaging than by the temporal averaging, which can be attributed to the much sparser spatial coverage of FC fluxes compared with ERBE. Thus the scatter of the differences in ERBE and FC values of $S\uparrow_t$ represents the true uncertainties of daily mean regional values because of sampling, rather than systematic errors.

The decrease in the standard deviation of the differences between daily and monthly mean values of $S\uparrow_t$ (Table 5) is less than expected for about 10-15 independent samples in one month (assuming correlations over synoptic time scales), indicating that monthly differences are affected by some systematic effects. Even smaller changes in differences between daily and monthly mean values of

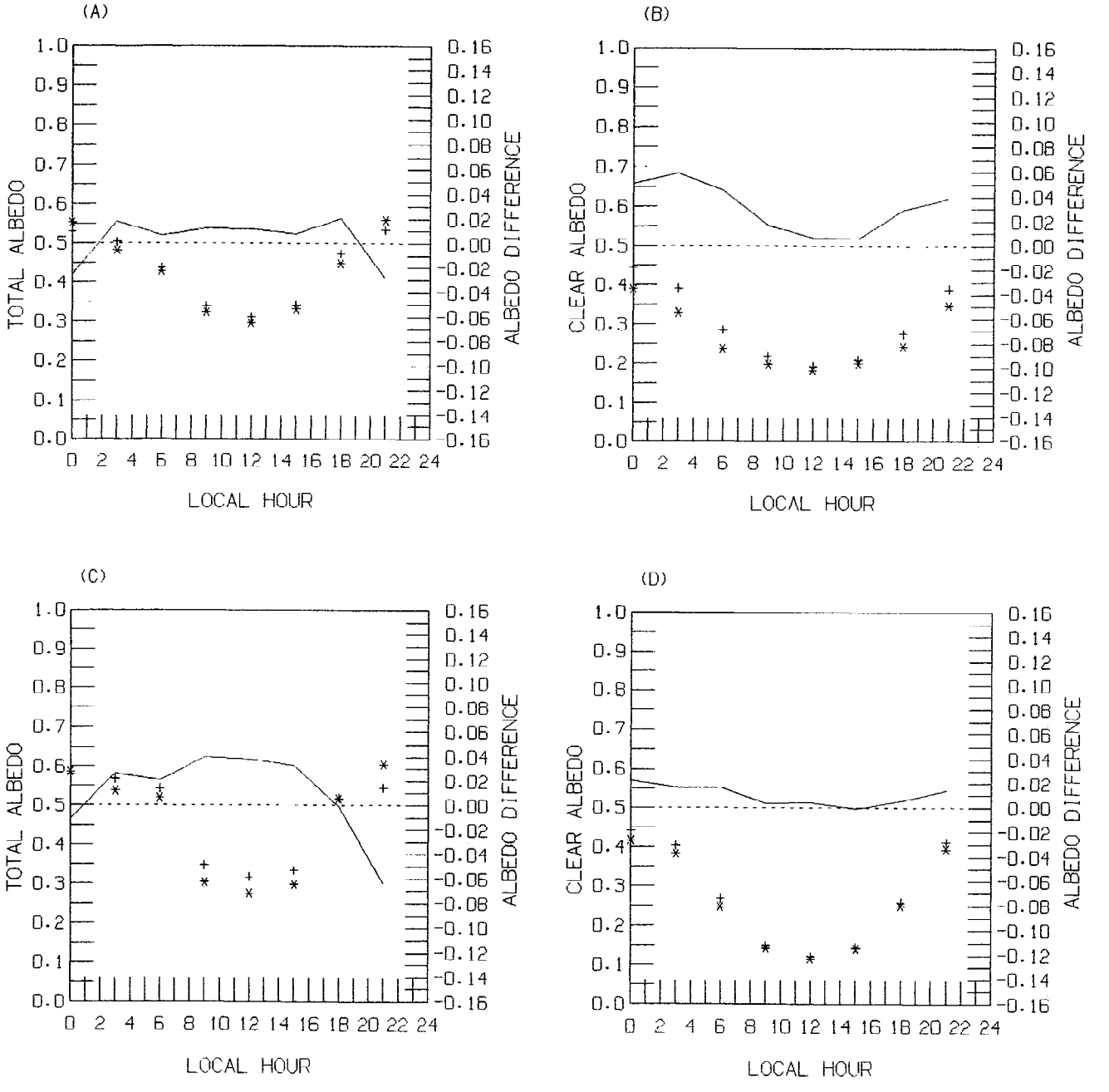

Figure 1. Global, monthly mean variations with local time of day of top of atmosphere albedos (left scale) for July 1986 from Earth Radiation Budget Experiment (ERBE) (asterisks) and Flux-Cloud data set (FC) (pluses) for (a) full sky over land, (b) clear sky over land, (c) full sky over ocean, and (d) clear sky over ocean. Albedo values at local nighttime hours are from the illuminated polar regions. Solid line indicates differences, FC minus ERBE, on the right scale.

CLR-$S\uparrow_t$ (not shown) suggest that some of the systematic difference in $S\uparrow_t$ values is associated with differences in clear-sky (surface) albedos. Figure 4 shows scatterplots of monthly mean map grid values of $S\uparrow_t$ and CLR-$S\uparrow_t$ for July 1986. Although the scatter is not large (normal deviations < 8 W/m²; see Table 4), the FC values are systematically higher in the middle range and lower in the highest range. Comparing Figures 4a and 4b shows that the CLR-$S\uparrow_t$ differences parallel the $S\uparrow_t$ differences. Most of the large values of $S\uparrow_t$ (and the large differences) are from the polar regions. *Hartmann and Doelling* [1991] note similar systematic regional biases in ERBE values of CLR-$S\uparrow_t$: values that appear to be too low by about 15 – 20 W/m² over the Amazon and values that appear to be too high by about 20 – 30 W/m² over Greenland and the Arctic [cf. *Stephens and Greenwald,* 1991a].

To look for systematic causes of disagreements in values of $S\uparrow_t$, we examined the average distribution of differences between FC and ERBE values as functions of ISCCP physical parameters: (1) surface temperature, visible reflectance, and total albedo; (2) cloud optical thickness, top temperature, and amount; (3) column precipitable water and ozone amount; and (4) solar zenith angle and latitude. Of these the only quantity that changes in a correlated fashion with the SW flux differences (correlation > 0.96 for July

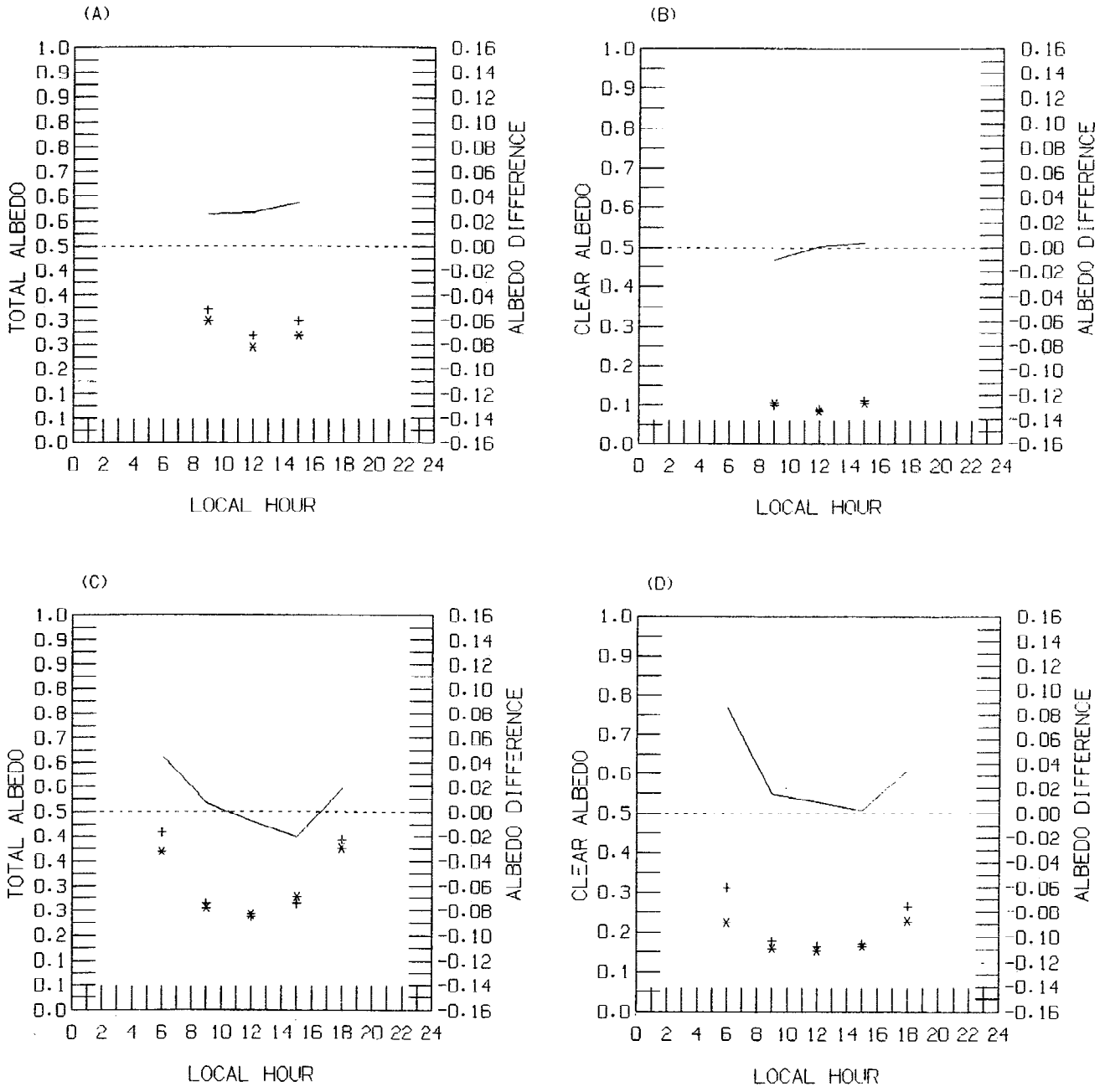

Figure 2. Same as Figure 1 but for two regions: (a) and (b) marine stratus (25°N to 40°N, 115°W to 135°W) and (c) and (d) central United States (30°N to 45°N, 80°W to 110°W).

1986 and January 1987) is cloud amount. As cloud amount increases from 0 to 100%, the average difference of $S\uparrow_t$ (FC – ERBE) increases linearly from about zero to about 10 W/m². Since the ERBE angular models are directly dependent on cloud amount, this suggests a small difference in the angular distribution of radiation in the two analyses and suggests that the overall higher FC planetary albedo is partly explained by this angle dependence difference.

In an earlier version of our calculations the differences of CLR-$S\uparrow_t$ were found to be correlated with the assigned spectral ratios between visible and near-IR albedos; hence we adjusted these ratios by comparison with the ERBE observations for land areas without snow or ice in the final version of the calculations [*Zhang et al.*, this issue]. Nevertheless, global maps of the remaining differences of CLR-$S\uparrow_t$ show a few land locations with values > 20 W/m².

Longwave (LW) fluxes. Examination of the average diurnal variations of $L\uparrow_t$ from FC and ERBE (Figure 5) shows even better quantitative agreement than for $S\uparrow_t$ (average differences are < 4 W/m² for full sky $L\uparrow_t$ and < 10 W/m² for clear sky with standard deviations < 10 W/m²); however, the ERBE diurnal cycles over land areas are nearly symmetric about local noon, whereas the FC results show significant shifts of the times of minimum and maximum values toward later times of day, particularly for summer clear sky conditions over land. Figure 6 highlights this difference for central United States in July 1986, where the daily maximum of CLR-$L\uparrow_t$ occurs between 1200 and 1500 LT (the FC results represent 3-hour averages) and the daily minimum occurs near 0600, consistent with other inferences of the diurnal surface temperature cycle [e.g., *Sellers*, 1965; *Minnis and Harrison*, 1984a, *Wetzel et al.*,

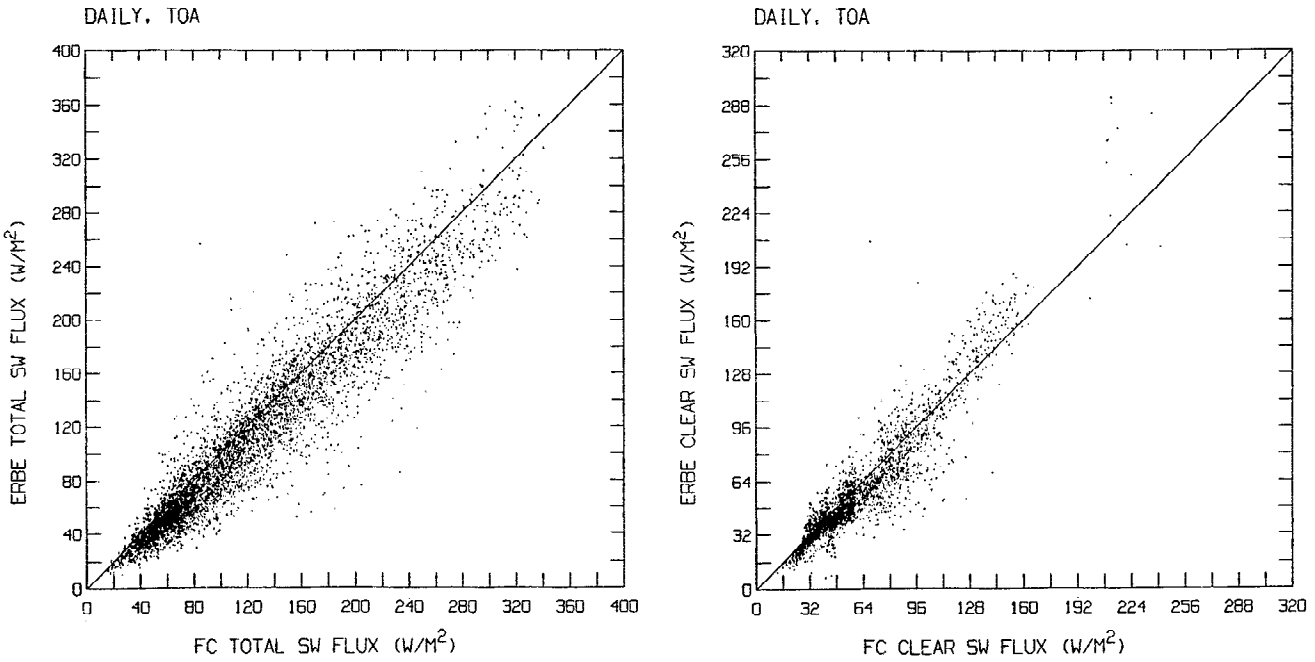

Figure 3. Scatterplot of individual equal-area map grid values of daily mean (a) $S\uparrow_t$ and (b) CLR-$S\uparrow_t$ in watts per meter square from ERBE (ordinate) and FC (abscissa) for July 15, 1986. Solid line indicates perfect agreement.

1984]. The afternoon-evening peak in summertime convective cloudiness eliminates (actually, slightly reverses) the diurnal asymmetry in full-sky $L\uparrow_t$. The ERBE values of $L\uparrow_t$ are based on direct measurements, though the diurnal cycle is sparsely sampled, but the CLR-$L\uparrow_t$ values are even more sparsely sampled (only under clear-sky conditions) and therefore more dependent on the diurnal model used to fill in missing values. Figures 5 and 6 show that while the ERBE $L\uparrow_t$ exhibit diurnal variations similar to the FC values, the ERBE diurnal ("half sine") model makes the CLR-$L\uparrow_t$ cycle too symmetric about local noon [cf. *Brooks and Minnis,* 1984a] compared with the 8 times daily FC results. Over oceans there is only a small (± 3 – 4 W/m²) diurnal cycle (Figure 5); but even in the western Pacific where the diurnal cycle of deep convective clouds is larger [e.g., *Fu et al.,* 1990], diurnal variations of $L\uparrow_t$ are small (Figure 6). In these cases the ERBE and FC results agree well, except for a systematic difference in CLR-$L\uparrow_t$. Note that the

Table 4. Comparison of Daily Mean ERBE and FC Fluxes for July 15, 1986, and January 15, 1987, and Monthly Mean ERBE and FC Fluxes for the Same Months

	July 15, 1986				January 15, 1987			
	$S\uparrow_t$	CLR-$S\uparrow_t$	$L\uparrow_t$	CLR-$L\uparrow_t$	$S\uparrow_t$	CLR-$S\uparrow_t$	$L\uparrow_t$	CLR-$L\uparrow_t$
Mean difference	11.5	4.3	0.4	-7.2	10.2	1.6	0.0	7.1
Standard deviation	20.0	11.0	13.7	9.7	20.9	12.9	14.2	10.4
Correlation coefficient	0.9555	0.9498	0.9489	0.9741	0.9618	0.9823	0.9504	0.9771
Slope	0.941	1.013	1.094	1.153	0.950	1.075	1.123	1.196
Interception	-4.8	-5.0	-22.8	-32.1	-4.3	-6.3	-28.6	-42.5
Normal deviation	14.2	7.7	8.9	5.5	14.9	8.2	8.9	5.2
Number of points	6178	3122	6590	4836	6554	3837	6590	5302
	July 1986				January 1987			
	$S\uparrow_t$	CLR-$S\uparrow_t$	$L\uparrow_t$	CLR-$L\uparrow_t$	$S\uparrow_t$	CLR-$S\uparrow_t$	$L\uparrow_t$	CLR-$L\uparrow_t$
Mean difference	10.2	4.7	0.2	-7.6	11.0	4.0	-0.8	-7.5
Standard deviation	9.4	10.0	7.8	8.3	9.7	12.4	7.9	8.3
Correlation coefficient	0.9854	0.9583	0.9820	0.9811	0.9890	0.9707	0.9857	0.9879
Slope	0.998	1.003	1.112	1.153	0.981	1.039	1.152	1.188
Interception	-10.0	-4.8	-26.9	-32.2	-8.7	-6.3	-34.4	-40.2
Normal deviation	6.6	7.1	4.6	4.4	6.8	8.5	4.0	3.6
Number of points	6434	6141	6590	6215	6492	6327	6590	6321

Quantities shown are derived from scatterplots of matched ERBE values (ordinate) and FC values (abscissa) and least squares linear fits. Differences are for FC minus ERBE. The normal deviation is the rms distance between each point and the linear fit. The number of values in each plot is also indicated. All quantities are in W/m² except correlation coefficient, regression line slope, and the number of points.

Table 5. Same as Table 4 but Comparing Differences Between ERBE and FC Fluxes Averaged Over 2.5° x 2.5° and 1 day (July 15, 1986), 2.5° x 2.5° and 1 month (July 1986), 10° x 10° and 1 day, and 10° x 10° and 1 month

	Daily: July 15 1986				Monthly: July 1986			
	$S\uparrow_t$		$L\uparrow_t$		$S\uparrow_t$		$L\uparrow_t$	
	2.5°	10°	2.5°	10°	2.5°	10°	2.5°	10°
Mean difference	11.5	-7.7	0.4	-14.5	10.2	-7.4	0.2	-14.4
Standard deviation	20.0	6.4	13.7	2.8	9.4	5.9	7.8	2.5
Correlation coefficient	0.9555	0.9995	0.9489	0.9993	0.9854	0.9998	0.9820	0.9996
Slope	0.941	1.074	1.094	1.052	0.998	1.076	1.112	1.051
Interception	-4.8	-1.0	-22.8	2.9	-10.0	-1.3	-26.9	2.96
Normal deviation	14.2	1.8	8.9	1.2	6.6	1.1	4.6	0.9
Number of points	6178	595	6590	648	6434	621	6590	648

magnitude of errors in $L\uparrow_t$ caused by errors in surface temperature is very small (< 2 W/m² global mean) because of the opacity of the atmosphere [*Zhang et al.*, this issue].

The ERBE clear sky values are systematically higher than the FC values over summer land by about 5 W/m² (diurnal model effect) and over all oceans by almost 8 W/m² (Figure 5). *Harrison et al.* [1990] report daytime biases of 6 W/m² in ERBE values of CLR-$L\uparrow_t$ over midlatitude land areas and nighttime biases of 6 – 7 W/m² over oceans; but they claim that the daily mean bias should be no more than 3 W/m². *Stephens and Greenwald* [1991a] find that ERBE CLR-$L\uparrow_t$ values are larger than Nimbus 7 values by about 5 W/m² at all latitudes. *Hartmann and Doelling* [1991] show high biases in ERBE values of CLR-$L\uparrow_t$ over tropical land areas of about 5 – 15 W/m². A bias in our calculations caused by the TOVS water vapor abundances is possible [cf. *Wittmeyer and Vonder Haar*, 1994], but the sensitivity of the calculated $L\uparrow_t$ limits this effect to < 5 W/m² [*Zhang et al.*, this issue].

Figure 7 shows a scatterplot of daily mean values of $L\uparrow_t$ and CLR-$L\uparrow_t$ from ERBE and FC results for July 15, 1986, and Table 4 summarizes the statistics of the comparison from July 15, 1986, and January 15, 1987. For full-sky conditions, the two data sets differ by < 1 W/m² with a standard deviation 13 W/m²; however, for clear-sky conditions, the mean difference changes from -7 to +7 W/m² from July 15 to January 15 with a standard deviation of about 10 W/m² (but the monthly mean difference is consistently -7 W/m² for both months). The correlations and regression fits indicate a more systematic difference between the ERBE and the FC values of $L\uparrow_t$ than for $S\uparrow_t$, although the magnitude of the differences is smaller (normal deviations of about 5 W/m²). Figure 8 shows an example of the scatterplot of monthly mean values of $L\uparrow_t$ and CLR-$L\uparrow_t$. At the high end, the ERBE values are systematically higher than the FC values and are associated with similar differences in CLR-$L\uparrow_t$.

Two kinds of regions show systematically larger differences: North Africa and high-latitude land areas in winter. The North Africa differences may be caused by the effect of a very symmetric diurnal model in ERBE and by seasonally constant clear-sky values used in the ERBE analysis [*Hartmann and Doelling*, 1991]. Another possibility is that the vertical distribution of water vapor, provided in the TOVS data set, is not accurate over areas with very large surface temperatures. The high-latitude discrepancies, particularly notable over Antarctica, may be caused by difficulties in identifying clear scenes in both the ISCCP and ERBE analyses. However, the high bias of our LW fluxes appears to be partly caused by the use of the U.S. Standard Atmosphere (1976) to specify humidities above levels at which the TOVS products provide values. This procedure

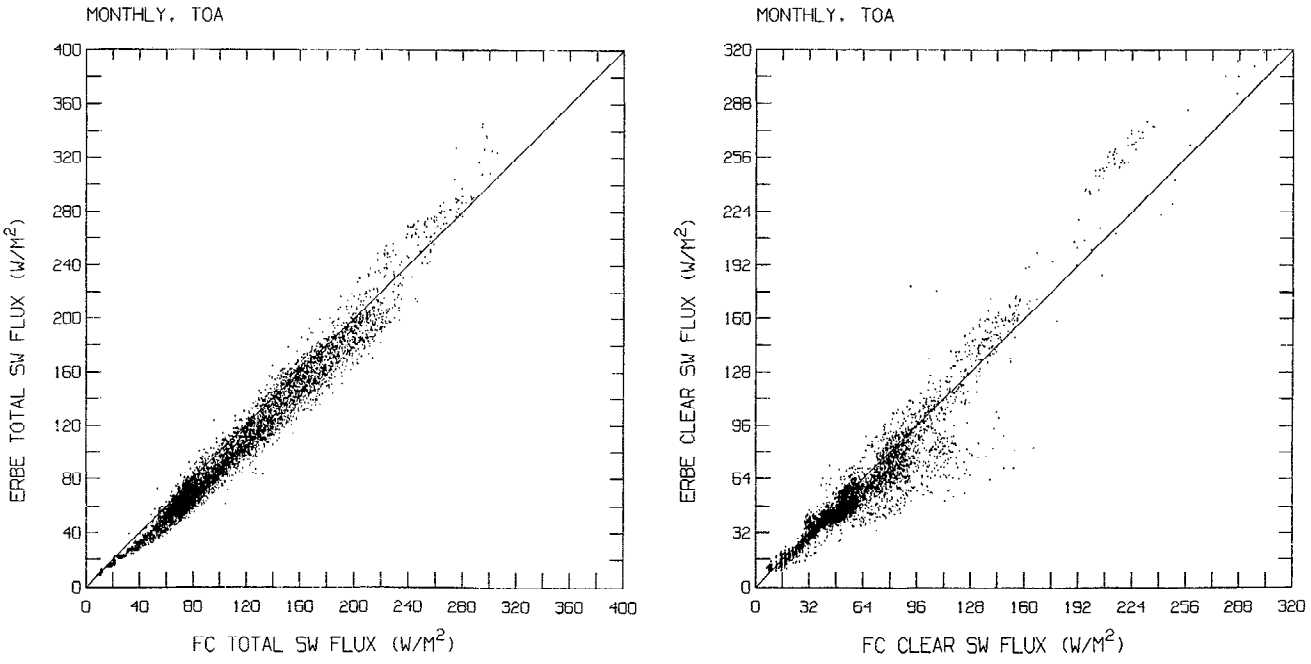

Figure 4. Same as Figure 3 but for monthly mean values of (a) $S\uparrow_t$ and (b) CLR-$S\uparrow_t$ in W/m².

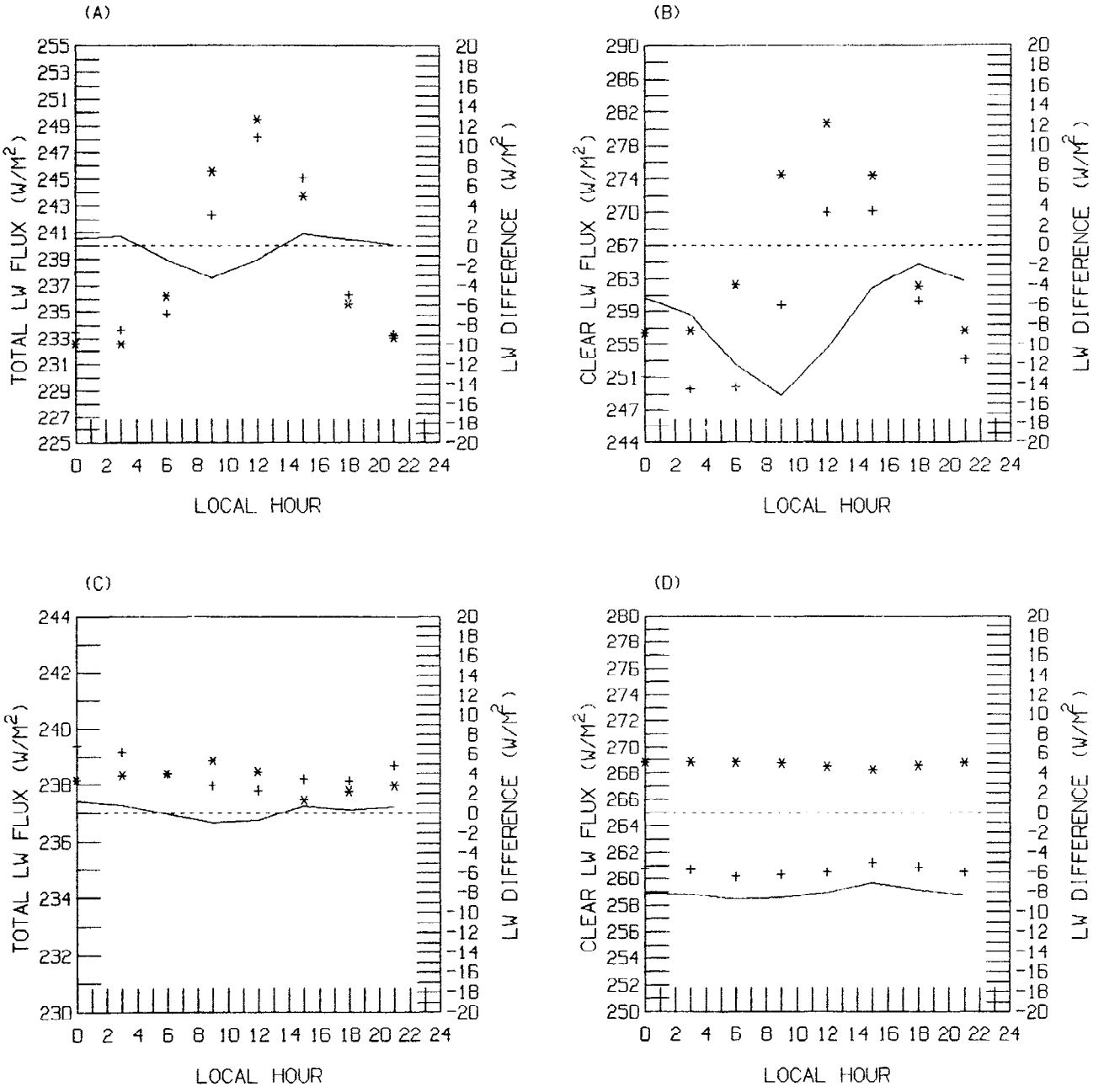

Figure 5. Same as Figure 1 but for $L\uparrow_t$ in W/m².

makes upper tropospheric humidities constant with latitude and season, causing an overestimate in polar wintertime. Even though specific humidities are very low over Antarctica in winter, the LW emission of the atmosphere is very sensitive to changing emissivity.

To look for systematic causes of disagreements in values of $L\uparrow_t$, we examined the average distribution of differences between FC and ERBE values as functions of the ISCCP physical parameters: (1) surface temperature, visible reflectance, and total albedo; (2) cloud optical thickness, top temperature, and amount; (3) column precipitable water and ozone amount; and (4) solar zenith angle and latitude. No systematic relationship of LW flux differences and physical parameters, including surface temperature and water vapor abundance, was apparent. Rather, the larger differences occur in specific locations suggesting that the particular conditions of the surface or clouds in these places produce differences in the ISCCP and ERBE analyses.

3.2. Surface Flux Measurements

The effects of differences in space-time sampling between satellite-based and surface measurements are even larger because most surface flux data sets are monthly averages of measurements from single fixed "points" (the view of the sky from the surface represents an area about 60 km across), whereas our surface fluxes are calculated for 2.5° × 2.5° equal-area map cells based on about 50 samples that cover only about 3% of the area. To check the effects of sampling, we compare multiple, closely spaced surface observations with high time resolution (1 min) and our calculated fluxes for a sample of individual satellite pixels (called FCX data).

The instruments used to measure radiative fluxes at the surface cover different spectral ranges than our calculated fluxes and this difference can introduce small biases in the comparisons. Typical pyranometers measure total SW radiation received at the surface in the wavelength range from about 0.28 to about 2.8 μm, whereas

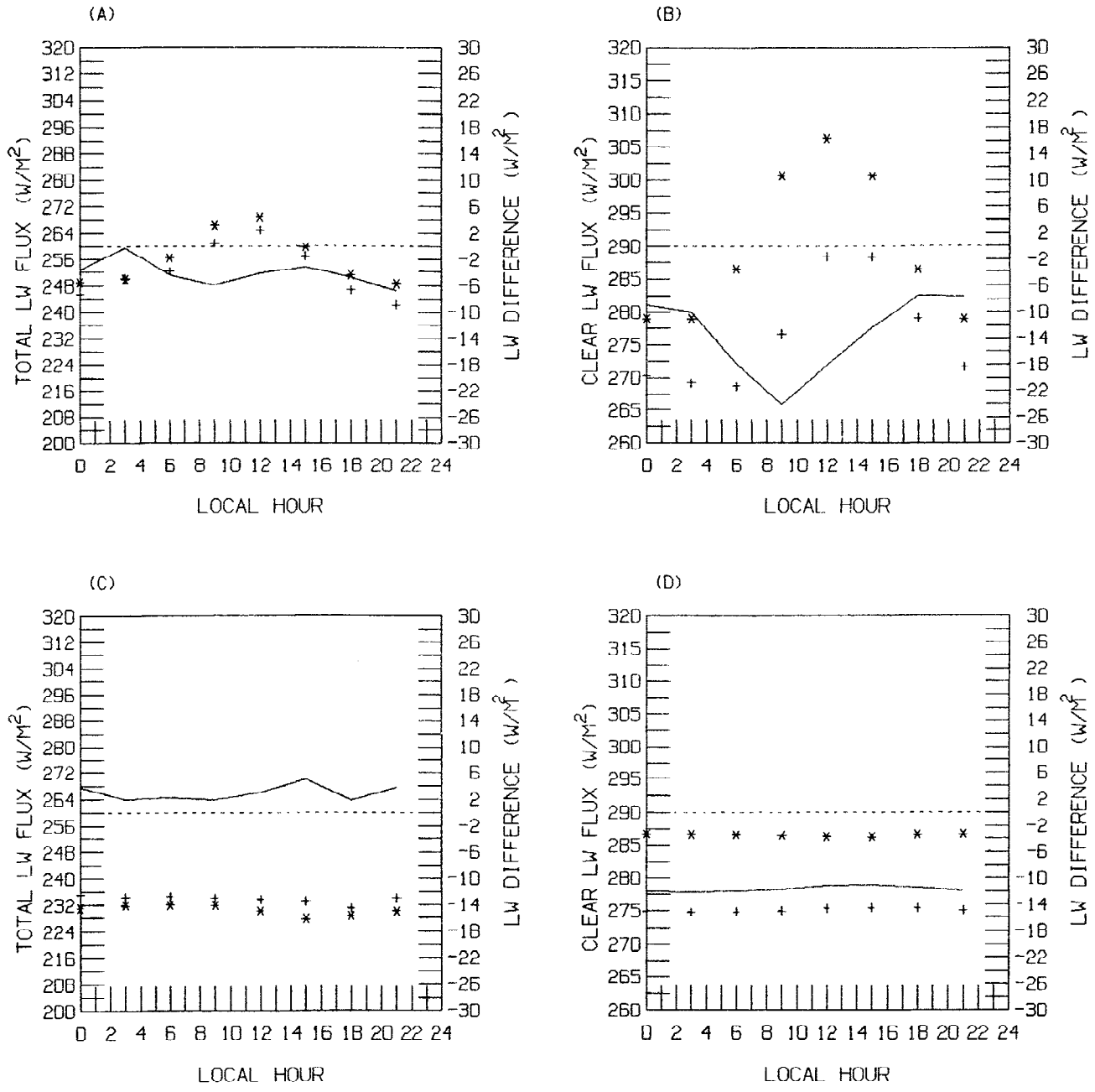

Figure 6. Same as Figure 2 but for two regions: (a) and (b) tropical convection over ocean (15°S to 15°N, 145°E to 180°E) and (c) and (d) central United States (30°N to 45°N, 80°W to 110°W).

our calculated SW fluxes represent the range 0.20 – 5.0 μm. Although this effect is partially accounted for in the calibration of standard pyranometers, the correction factor varies with the altitude of the calibration site and an underestimate of as much as 1-2% in surface SW fluxes is still possible (C. Fröhlich, private communication, 1993). For example, during the Wisconsin surface radiation experiment, described below, two sets of pyranometers with calibrations performed by two different centers (at different altitudes) differed by 3% when the instruments were compared side by side [*Whitlock et al.*, 1990b]. Likewise most pyrgeometers measure LW fluxes in the wavelength interval from about 4.0 to about 50 μm, whereas our calculated LW fluxes represent the range 5.0 – 200.0 μm. At air temperatures above 250 K this difference may cause an underestimate of as much as 1% in surface measurements.

First ISCCP Regional Experiment /Surface Radiation Budget (FIRE/SRB) 1986. FIRE conducted its first field campaign in Wisconsin during a 3-week period (October 12 to November 2, 1986) to study cirrus clouds [*Cox et al.*, 1987]. As part of preparations for an international Surface Radiation Budget (SRB) project, surface flux measurements were also made to provide validation data for satellite-based surface flux algorithms [*Whitlock et al.*, 1990a]. Values of $S\downarrow_s$ were measured every minute at 17 sites from 1200 to 2400 UTC by a mixture of Eppley model PSP and Kipp and Zonen CM5 pyranometers [*Whitlock et al.*, 1990b]. The Eppley PSP instruments were calibrated by NOAA Environmental Research Laboratories (ERL), which is the World Meteorological Organization (WMO) regional radiation center in the United States. The Kipp and Zonen CM5 instruments were calibrated by Atmospheric

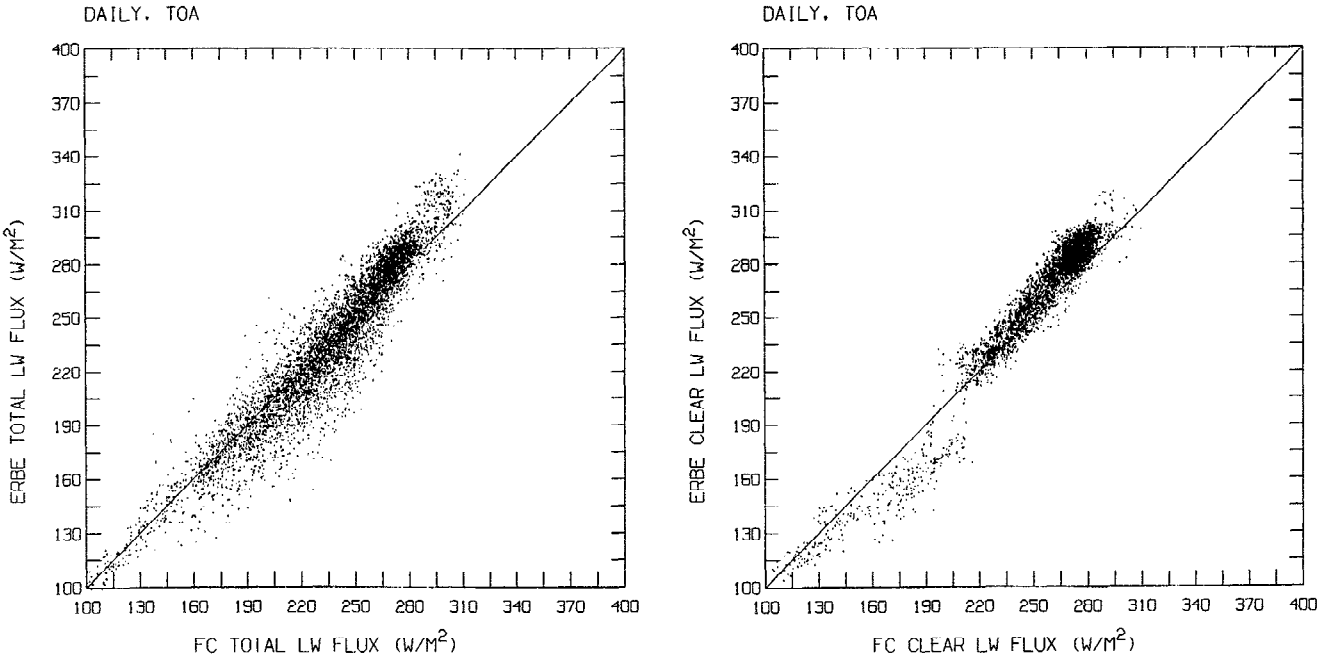

Figure 7. Same as Figure 3 but for daily mean values of (a) $L\uparrow_t$ and (b) CLR-$L\uparrow_t$ in W/m².

Environment Services (AES), the WMO regional radiation center in Canada. Representative instruments were compared at the same site before data collection began; all results from the Kipp and Zonen CM5 instruments were reduced by 3% to be consistent with the results from the Eppley PSP instruments [*Whitlock et al.*, 1990b]. Values of $L\downarrow_s$ were measured every minute at five sites from 0000 to 2359 UTC by Eppley model PIR pyranometers [*Whitlock et al.*, 1990c]. All PIR instruments were calibrated by AES of Canada as a World Meteorological Organization (WMO) regional radiation center. They were also compared to another Eppley PIR calibrated and operated by Colorado State University [*Albrecht and Cox*, 1977] and found to give LW flux values within a few watts per square meter. All sites are shown in Figure 9, together with the positions of the nearest satellite pixels obtained from the spatially sampled ISCCP data sets [*Schiffer and Rossow*, 1985]. For comparison with our satellite-based flux values, the 1-minute time records are averaged over 30-minute periods centered on the estimated time at which the satellite measurements were made over each site. We also tried averages over 1, 15, 30, and 60 min, but the results are not too sensitive to the choice of time averaging. For typical windspeeds of 10-15 m/s, an average over 30-minute corresponds to a spatial scale of 15-30 km, similar to the sampling interval of the satellite pixels in the ISCCP data sets and to the uncertainty of pixel location.

Our values of $S\downarrow_s$ and $L\downarrow_s$ are calculated using both the ISCCP

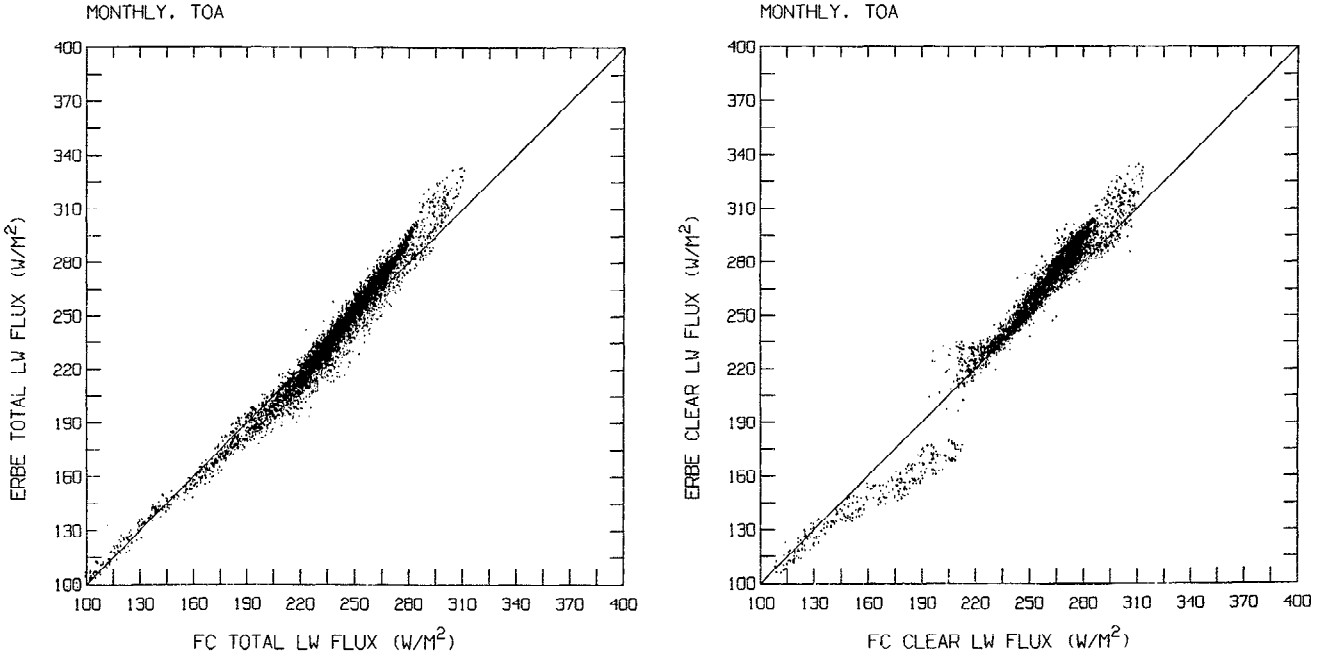

Figure 8. Same as Figure 7 but for monthly mean values of (a) $L\uparrow_t$ and (b) CLR-$L\uparrow_t$ in W/m².

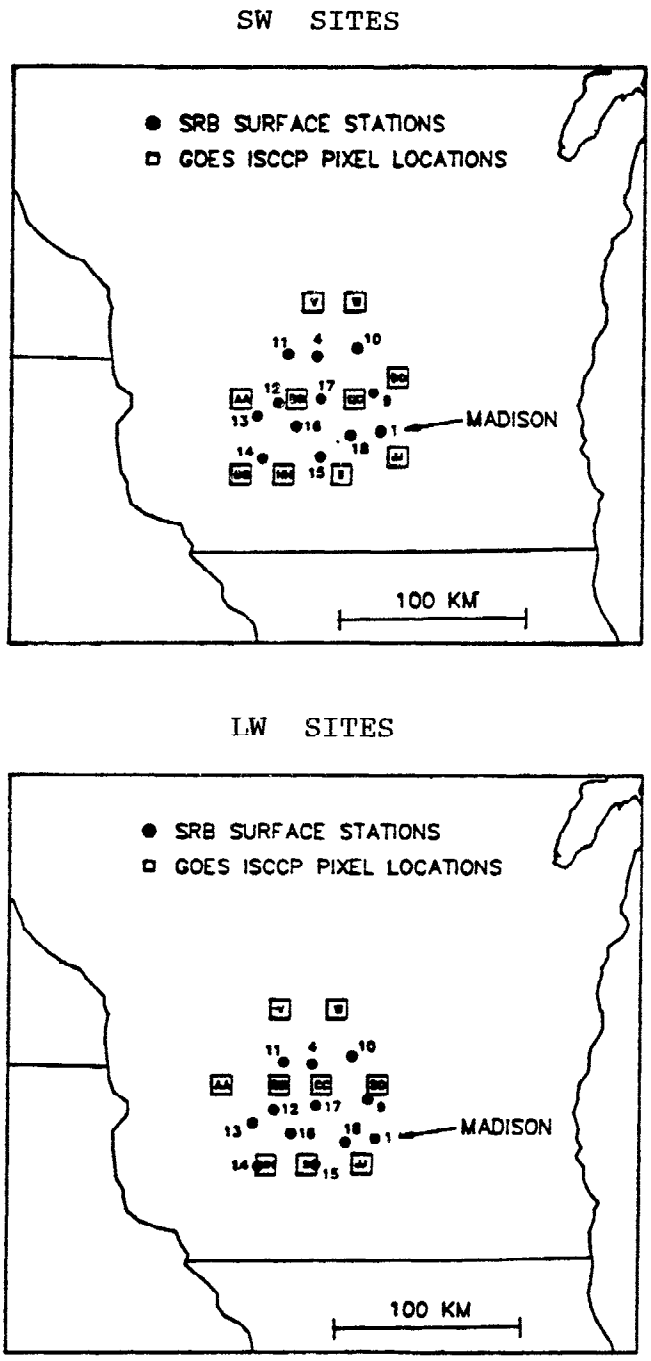

Figure 9. Map of Wisconsin experiment area showing location of shortwave (SW) flux and longwave (LW) flux surface sites and the International Satellite Cloud Climatology Project (ISCCP) CX pixels used for calculating surface radiative fluxes.

C1 data set from the two map grid cells containing the Wisconsin sites (FC result) and the closest individual satellite pixels from the ISCCP CX data set (FCX result). The solar zenith angles used for FCX values are the instantaneous values instead of the 3-hour averages used for FC. There are a total of 21 days of matched data available for comparison.

We compare matched FCX and surface values of $S\downarrow_s$ in four ways (Table 6): (1) at individual times for each surface measurement site; (2) area-averaged values at individual times; (3) daily mean values for each individual site; and (4) daily and area-averaged values. For daily mean values from satellite, where the diurnal sampling is incomplete, the individual values are weighted by the ratio of the sum of cosines of the solar zenith angle (μ_0) over a whole day and the actual sum of μ_0 values for the available observations [cf. *Bishop and Rossow,* 1991]. Daily mean values for the surface observations are calculated using the whole 1-minute measurement record, but if data are missing, then the remaining values are weighted by a μ_0-sum ratio. Statistics from all of these comparisons are listed in Table 6, together with equivalent comparisons for the FC results.

We argue that much of the scatter in the differences between the satellite-based and the surface-based measurements of $S\downarrow_s$ is caused by their different space/time sampling of the spatial and temporal inhomogeneities of $S\downarrow_s$. This explanation is supported by the progressive decrease in the standard and normal deviations of the differences between the FCX and the surface values as the observations are averaged over ever larger space and time domains (Table 6). Moreover, the normal deviation of the differences of FC and individual FCX results is 32.0 W/m², almost as large as the differences between FC and individual surface measurements (45.2 W/m²). However, the normal deviation (excluding bias) decreases about half as much as expected if all the samples were independent samples (i.e., by $1/\sqrt{N}$, where N is the number of samples shown at the bottom of Table 6), indicating that significant flux variability caused by clouds occurs on scales larger than about 100 km and one day. (Note that part of the decrease when daily mean values are computed occurs simply because averaging over 24 hours includes zero values for nighttime.) The daily and area-average values of $S\downarrow_s$ from FCX agree very well with the surface measurements (Table 6 and Figure 10a): the mean and normal deviation of their differences (FCX minus surface measurements) are 8.4 and 6.5 W/m², respectively, the correlation is 0.98, and the regression slope is 0.93. The comparison with FC data is about the same (Table 6) with a normal deviation of 10.0 W/m².

The averaged FCX value of $S\downarrow_s$ is about 8 W/m² higher than measured at the surface, primarily because the larger FCX values in Figure 10a (> 140 W/m² daily mean), which correspond to clear, broken cloud or thin overcast cloud conditions (according to surface observers), are larger than measured at the surface. The average FC value of $S\downarrow_s$ is about 12 W/m² lower than the average FCX value indicating some systematic difference in the mean conditions occurring in the larger area encompassed by the two FC map grid cells than occurring right over the Wisconsin sites. The difference of the FCX value of $S\downarrow_s$ is < 4 W/m² under thick overcast cloud conditions. This behavior explains a regression slope < 1 and indicates that the cause of the systematic SW flux difference is associated with the clear atmosphere rather than the clouds. Table 6 shows that the bias is even larger and the regression slope even smaller when comparing instantaneous fluxes (excluding nighttime values).

Two factors can contribute to this type of discrepancy. The background aerosol optical thickness used in the calculations is 0.16, which could well be a significant underestimate for a region with significant human activity. *Husar et al.* [1981], for example, reports average haze visible optical thicknesses between 0.2 and 0.3 for Wisconsin for the period 1961 – 1975, with considerable seasonal (± 40% amplitude) and interannual (± 50% amplitude) variability and some suggestion of an increasing trend. An increase of aerosol optical thickness to 0.3 in our calculations would decrease the daily mean clear sky $S\downarrow_s$ by about 3 W/m². The second factor is the difference in spectral ranges covered by the calculated and measured values of $S\downarrow_s$, which could account for a bias of 2 – 5 W/m². Since the difference occurs at wavelengths > 2.5 μm that are strongly absorbed by clouds, this factor would introduce a bias

Table 6. Same as Table 4 But Comparing FCX and FC Values of $S\downarrow_s$ and $L\downarrow_s$ With Direct Surface Measurements From a Surface Site Array in Wisconsin for October 14 to November 2, 1986, During FIRE Cirrus I Experiment [*Whitlock et al.* 1990a, b, c]

FCX Comparison	$S\downarrow_s$				$L\downarrow_s$			
	1	2	3	4	1	2	3	4
Mean difference	13.9	14.1	8.6	8.4	-8.6	-8.6	-8.8	-9.6
Mean difference, %	7.9	8.1	7.9	7.7	-2.8	-2.8	-2.8	-3.1
Standard deviation	57.3	35.5	16.3	9.5	35.6	30.1	26.9	21.9
Correlation coefficient	0.9586	0.9844	0.9481	0.9822	0.5747	0.6518	0.6741	0.7718
Slope	0.897	0.919	0.910	0.934	0.770	0.912	0.963	1.061
Interception	4.1	-0.1	1.2	-1.2	80.4	36.1	20.3	-9.5
Normal deviation	39.8	23.4	11.5	6.5	27.6	22.1	19.4	15.0
Normal deviation, %	22.7	13.5	10.5	6.0	8.8	7.1	6.2	4.8
Number of points	1658	104	345	21	732	166	97	21
FC Comparison	$S\downarrow_s$				$L\downarrow_s$			
	1	2	3	4	1	2	3	4
Mean difference	-6.7	-6.5	-4.0	-4.0	-10.5	-10.1	-10.52	-11.8
Mean difference, %	-4.3	-4.3	-4.2	-4.2	-3.3	-3.2	-3.3	-3.7
Standard deviation	66.2	40.9	23.3	14.9	31.3	27.0	23.6	15.0
Correlation coefficient	0.9361	0.9759	0.8848	0.9532	0.5449	0.6191	0.6654	0.8775
Slope	1.052	1.072	1.013	1.063	0.874	0.951	1.008	1.254
Interception	-1.3	-4.4	2.7	-2.0	50.3	25.6	7.9	-69.1
Normal deviation	45.2	26.7	16.1	10.0	23.5	19.6	16.6	8.8
Normal deviation, %	29.5	17.6	16.9	10.6	7.4	6.2	5.3	2.8
Number of points	1509	95	311	19	661	152	87	16

FIRE is the First ISCCP Regional Experiment. Comparison 1 is for individual observations at each site and time; comparison 2 is for observations from each time but averaged over all sites; comparison 3 is for daily mean values at each site; and comparison 4 is for daily mean values averaged over all sites. Differences are for FCX or FC minus surface observations. Percentage differences are with respect to the average FCX or FC fluxes.

only for clear or nearly-clear conditions as we observe. Neither factor, alone, is sufficient to explain the whole bias, however.

Comparisons of $L\downarrow_s$ values are performed in the same ways as for $S\downarrow_s$ (Table 6). The mean and normal deviation of the differences of daily, area-mean values (FCX minus surface measurements) are -9.6 and 15.0 W/m², respectively. Figure 10b shows the comparison for daily and area-averaged values. Again, averaging both sets of observations over space and time reduces the scatter of their differences by about half as much as expected for independent samples, consistent with significant flux variations at larger space-time scales. However, the comparison between daily mean FC and the daily, area-averaged surface measurements exhibits less scatter

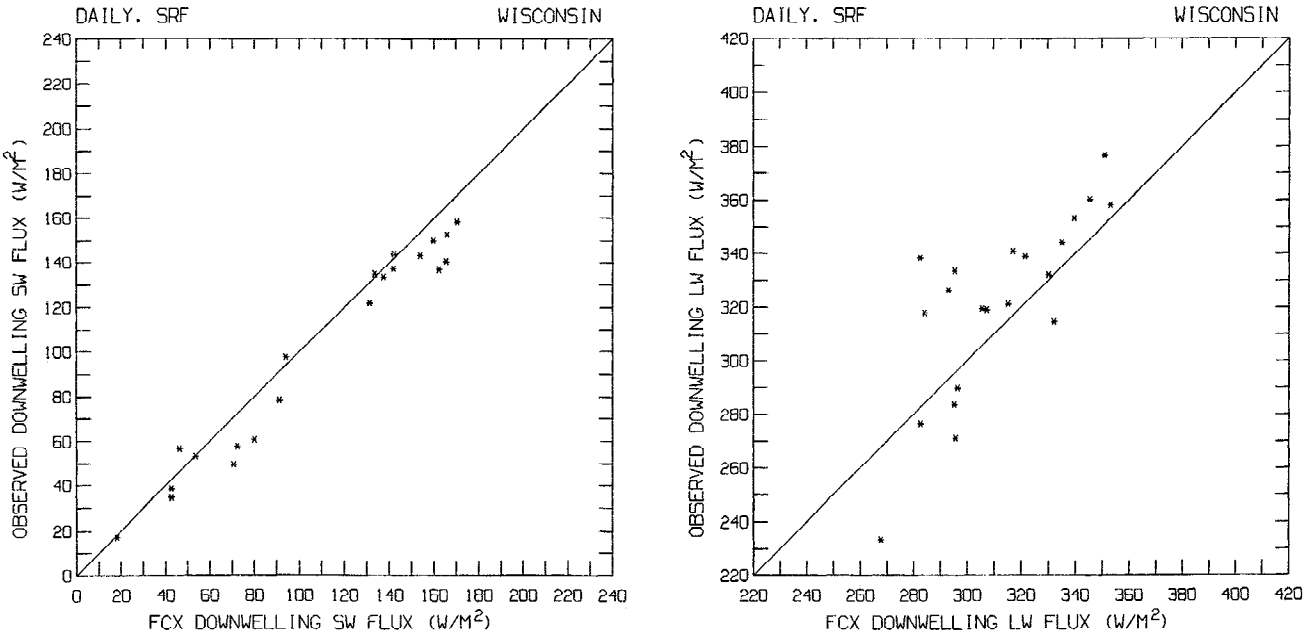

Figure 10. Same as Figure 3 but for daily and area averaged values of (a) $S\downarrow_s$ and (b) $L\downarrow_s$ in W/m² from FCX (abscissa) and measured (ordinate) at the surface in Wisconsin (see Figure 9).

than for daily, area-averaged FCX (Table 6). Since the only difference between FC and FCX is that the former has more samples for the area and time in question, the smaller scatter of differences with surface observations for FC results suggests that sampling does not account for all of the scatter in the comparing FCX and surface measurements.

This conclusion is reinforced by the facts that the correlation of daily and area-averaged values from FCX and the surface measurements is only 0.77, that the standard deviation of the FCX values is smaller than that of the surface values, and the slope of linear least squares fit is >1. Sensitivity studies show that only the atmospheric temperature variability is important enough to explain variations of the FCX values of $L\downarrow_s$ that are too small. Even doubling the amplitude of cloud base variations from about 140 to 280 mbar does not increase the variation of $L\downarrow_s$ by more than 1 – 3 W/m²; whereas doubling the variations of water vapor from about 25% to 50% only increases $L\downarrow_s$ variations by about 5 – 7 W/m². (Our estimated cloud base varied by about 140 mbar rms, which is actually slightly larger than surface observer estimates of cloud base height variations of about 800 m rms, equivalent to about 100 mbar.) The standard deviation of TOVS atmospheric temperatures is 1 – 2 K less than observations from nearby surface weather stations, mostly because the daily TOVS values do not capture the diurnal variability of temperatures. Thus the actual (including diurnal) variations in atmospheric temperature must be larger and the water vapor variations better correlated with temperature variations than represented by the daily TOVS data, increasing the variability of $L\downarrow_s$ by about 10 W/m² as compared to the calculated values. A small bias of our values can also be accounted for by increasing TOVS temperatures by about 1 K.

The Tropical Ocean-Global Atmosphere program – Coupled Ocean-Atmosphere Response Experiment (TOGA-COARE) pilot cruise 1990. Another detailed comparison of surface radiative fluxes, including $L\uparrow_s$, was conducted using "hourly"-mean observations from a 22-day pilot cruise in the TOGA-COARE region from February 16 to March 10, 1991 [*Young et al.*, 1992]. For this comparison, FCX values are calculated for the single satellite pixel nearest the ship position at each time. SW fluxes were calculated using 50-minute averages (centered on each hour) of solar zenith angle to match the time averaging of the surface observations [*Young et al.*, 1992]. Table 7 summarizes the comparison statistics for this case and Figure 11a shows the scatterplot for daily mean values of $S\downarrow_s$. The scatter of the differences between FCX and ship-measured values of $S\downarrow_s$ is more than 2 times larger in this case than for the Wisconsin comparison (Table 7), but the daily mean fluxes are also almost twice as large. The area-averaged satellite results (FC) exhibit as much scatter relative to the ship measurements as they do relative to individual FCX values, indicating that the quasi-random differences are mostly due to spatial sampling [*Sèze and Rossow*, 1991b]. The average difference of $S\downarrow_s$ values (21.5 W/m², FCX > ship) is also larger than in the Wisconsin results in direct proportion to the daily mean values of $S\downarrow_t$ and the slope of the best fit regression line has a smaller slope. Almost all of the difference occurs under clear or thin overcast cloud conditions. An increase of aerosol optical thickness by a factor of almost 5, from 0.045 to 0.218 (e.g., *Durkee et al.* [1991] show aerosol optical thicknesses > 0.1 in the western Pacific), decreases the FCX values of $S\downarrow_s$ by ≈ 6 W/m² and CLR-$S\downarrow_s$ by almost 10 W/m². An increase of all cloud optical thicknesses by 20% to correct a calibration bias [*Klein and Hartmann*, 1993] only reduces the bias by ≈ 4 W/m². The remaining

Table 7. Same as Table 6 But Comparing FCX and FC Values of $S\downarrow_s$ and $L\downarrow_s$ With Direct Surface Measurements From the TOGA Pilot Cruise Near the Equator in the Western Pacific From February 28 to March 10, 1990 [*Young et al.*, 1992]

FCX Comparison	$S\downarrow_s$		$L\downarrow_s$		$L\uparrow_s$	
	1	3	1	3	1	3
Mean difference	24.9	21.5	16.7	16.2	20.4	21.2
Mean difference, %	11.0	9.1	3.8	3.7	4.2	4.4
Standard deviation	122.1	40.8	16.8	13.5	14.5	12.3
Correlation coefficient	0.9154	0.8766	0.3048	0.5423	0.1574	0.4295
Slope	0.850	0.773	0.172	0.209	0.0142	0.0541
Interception	5.0	31.3	349.3	332.4	456.3	437.1
Normal deviation	86.3	28.5	9.3	5.0	2.4	1.4
Normal deviation, %	39.6	12.1	2.1	1.1	0.5	0.3
Number of points	135	22	135	22	135	22
FC Comparison	$S\downarrow_s$		$L\downarrow_s$		$L\uparrow_s$	
	1	3	1	3	1	3
Mean difference	30.8	24.5	16.3	15.9	21.9	23.2
Mean difference, %	13.0	10.0	3.7	3.6	4.5	4.8
Standard deviation	140.2	52.9	15.3	13.2	15.3	13.1
Correlation coefficient	0.8994	0.7068	0.3647	0.5699	0.2233	0.3463
Slope	0.883	1.012	0.213	0.223	0.0246	0.0422
Interception	-3.7	-27.3	331.2	326.5	451.3	442.8
Normal deviation	101.4	37.2	8.9	4.9	2.3	1.4
Normal deviation, %	41.9	15.6	2.0	1.1	0.5	0.3
Number of points	140	22	140	22	140	22

TOGA is the Tropical Ocean-Global Atmosphere program. Since observations are available only from one surface site, only comparisons 1 and 3 are made. Differences are for FCX or FC minus ship observations. Percentage differences are with respect to the average FCX or FC fluxes.

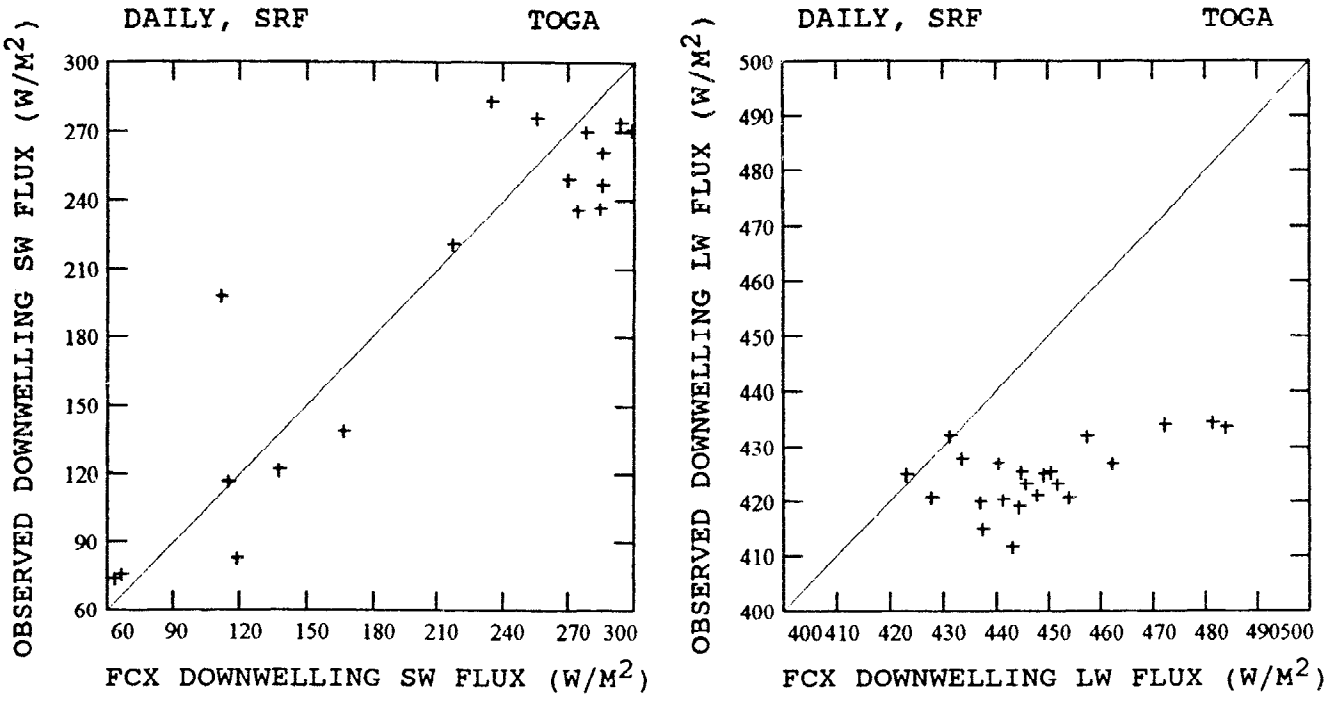

Figure 11. Same as Figure 10 but for daily mean values of (a) $S\downarrow_s$ and (b) $L\downarrow_s$ in W/m² from FCX and measured on a ship during the Tropical Ocean-Global Atmosphere program (TOGA) pilot cruise [*Young et al.*, 1992].

10 – 15 W/m² of this persistent discrepancy can be accounted for by the difference in spectral coverage between instruments used to measure SW fluxes at the surface and our calculations: a 2% bias in the surface measurements [*C. Fröhlich*, private communication, 1993] is sufficient.

Tropical conditions increase the importance of an accurate specification of atmospheric temperature and water vapor abundances and decrease the importance of cloud base locations to the determination of $L\downarrow_s$. In contrast with the Wisconsin case, the 5 W/m² scatter of differences between FCX and ship values of $L\downarrow_s$ (Figure 11b) is more than three times smaller in the TOGA case and does not increase when comparing area averages with a point measurement (Table 7), suggesting spatially and temporally uniform atmospheric conditions. Even so, the FCX values exhibit much more day-to-day variability than the surface observations producing a correlation of day-to-day variations of only 0.54 and a regression slope of 0.21 (Figure 11b). Recalculation of $L\downarrow_s$ values using the atmospheric temperature variability observed on the ship, which is half of the TOVS variability, reduces $L\downarrow_s$ variations to a magnitude similar to that measured by the ship radiometer [cf. *Zhang et al.*, this issue]. Although water vapor variations do not contribute to significant variations in $L\downarrow_s$, the TOVS variations are three times larger than measured on the ship and help to decrease the correlation of the two time records. Several different analyses of Special Sensor Microwave/Imager (SSM/I) measurements imply a bias of the TOVS water vapor abundances [cf. *Wittmeyer and Vonder Haar*, 1994], but this can only account for about 5 W/m² uncertainty in the calculated values of $L\downarrow_s$. However, the TOVS air temperature used in the calculations is about 2 K larger than the ship-measured near-surface air temperature, which can explain most of the bias in the calculated $L\downarrow_s$.

We also examined the accuracy of the ISCCP sea surface temperatures (SST), paying particular attention to differences between skin and bulk temperatures [*Wick et al.*, 1992] and the calculated values of $L\uparrow_s$. We considered the effects of using different atmospheric water vapor amounts from satellite microwave measurements for the SST retrievals. Even though the retrieved SST values are only about 1 K higher than the ship-measured values, the calculated values of $L\uparrow_s$ are about 20 W/m² higher than measured on the ship. Even with a slightly smaller SST, the calculated $L\uparrow_s$ is still about 8 W/m² larger than measured on the ship; but this remaining 2% difference in LW flux is well within the uncertainty of the ship instrument calibration.

Barrow and the south pole 1986. Table 8 shows comparisons of calculated (nearest-satellite pixel to each site at each time) and surface-measured values of $S\downarrow_s$ and $L\downarrow_s$ for sites at Barrow, Alaska, and at the south pole. Although the magnitudes of the flux differences (10 – 30 W/m² daily mean) are roughly similar to the Wisconsin and TOGA-pilot case studies, this is misleading because the mean values of the SW and LW fluxes are so small that even large errors in specifying cloud properties have little effect on the fluxes (see percentage magnitudes in Tables 6 – 8). Sensitivity studies of the Barrow case show that variations in the calculated values of $S\downarrow_s$ depend mostly on variations of solar zenith angle and cloud amount. Although the ISCCP results provide cloud amounts at all times, too low illumination precludes determining cloud optical thicknesses during most of October. Thus the high correlation of calculated and measured variations of $S\downarrow_s$, shown in Figure 12a, is explained by a stronger dependence on solar zenith angle and cloud amount changes than on optical thickness changes. A change of average cloud optical thickness from 2 to 15 decreases the mean $S\downarrow_s$ by half, but this is only 15 W/m², and decreases the regression slope from what is shown in Figure 12a. Calculated and measured values of $L\downarrow_s$ are only weakly correlated due mostly to variations of TOVS temperatures (Figure 12b).

Sensitivity studies of the south pole case suggest that our cloud amount is too low, causing a 25 W/m² high bias in our $S\downarrow_s$ values [cf. *Dutton et al.*, 1991] that cannot be explained by varying other parameters (ozone, water vapor, aerosol) within reasonable limits. However, most of the variation is produced by solar zenith angle

Table 8. Same as Table 6 But Comparing FCX Values of $S\downarrow_s$ and $L\downarrow_s$ With Direct Surface Measurements at Barrow, Alaska, and at the South Pole for October 1986

Barrow, Alaska	$S\downarrow_s$		$L\downarrow_s$	
	1	3	1	3
Mean difference	10.0	6.3	-28.2	-29.2
Mean difference, %	24.1	25.1	-13.5	-14.0
Standard deviation	29.9	10.7	39.0	29.0
Correlation coefficient	0.8679	0.7028	0.2312	0.3416
Slope	0.648	0.456	0.379	0.532
Interception	4.6	7.4	157.4	127.1
Normal deviation	18.2	6.3	34.0	24.4
Normal deviation, %	43.9	25.1	16.3	11.7
Number of points	112	23	113	28
South Pole	$S\downarrow_s$		$L\downarrow_s$	
	1	3	1	3
Mean difference	25.4	25.3	30.3	30.2
Mean difference, %	15.7	15.1	22.7	22.7
Standard deviation	36.6	23.9	32.3	26.2
Correlation coefficient	0.9072	0.9603	-0.2179	-0.2661
Slope	0.790	0.867	-0.321	-0.561
Interception	8.7	-2.8	146.0	177.7
Normal deviation	24.9	16.0	22.6	18.1
Normal deviation, %	15.4	9.5	16.9	13.6
Number of points	227	28	232	31

Only comparisons 1 and 3 are made. Differences are for FCX minus surface observations. Percentage differences are with respect to the average FCX fluxes.

changes, so the calculated and measured values of $S\downarrow_s$ are even better correlated (Figure 13a) than at Barrow. Too low ISCCP cloud amounts at the south pole make them unimportant to the average value of $L\downarrow_s$ and cannot explain the high bias and nearly constant values of the FCX values of $L\downarrow_s$ (Figure 13b). The calculated values of $L\downarrow_s$ depend more on atmospheric temperature and water vapor amount: a factor of two decrease in TOVS water vapor amounts decreases $L\downarrow_s$ by about 25 W/m²; but a small reduction of atmospheric temperature can also account for the bias. The operational analysis of TOVS data rarely reports values over the high Antarctic plateau, so that the ISCCP processing substitutes climatological values [*Rossow et al.*, 1991] that are dominated by observations from coastal locations where water amounts and temperatures can be expected to be too large. In addition, our use of the U.S. Standard Atmosphere (1976) humidities in the upper troposphere adds to the overestimate of humidity and $L\downarrow_s$. The nearly constant value of $L\downarrow_s$

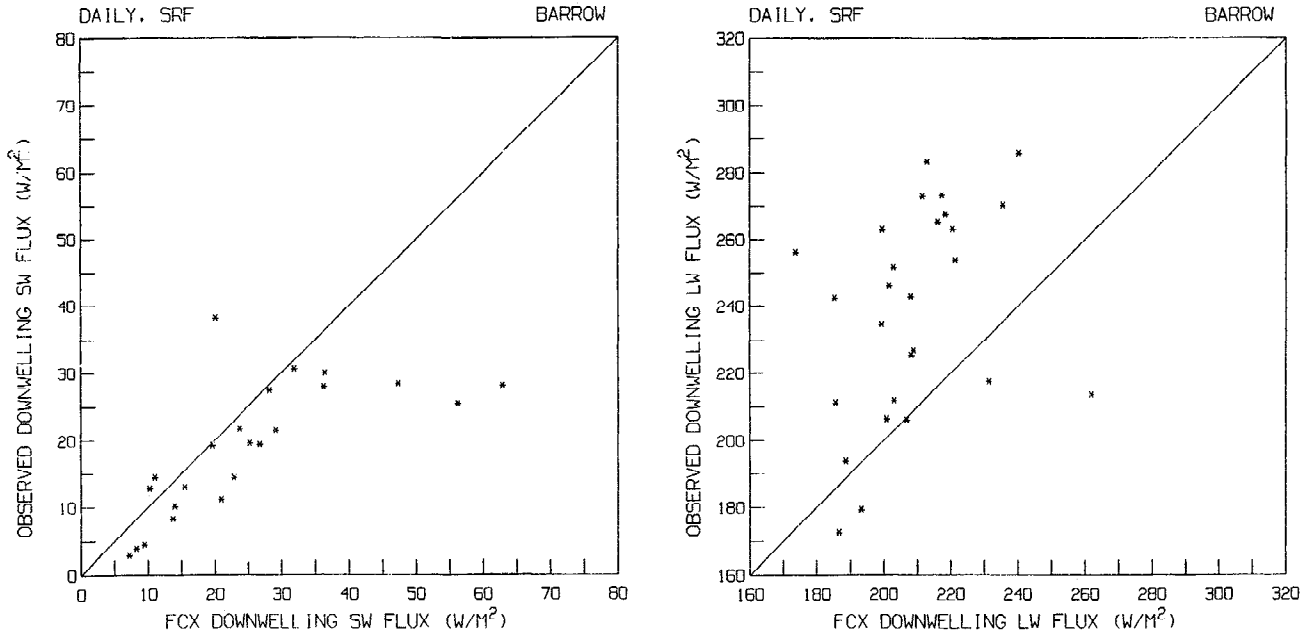

Figure 12. Same as Figure 10 but for daily mean values of (a) $S\downarrow_s$ and (b) $L\downarrow_s$ in W/m² from FCX and measured at Barrow, Alaska.

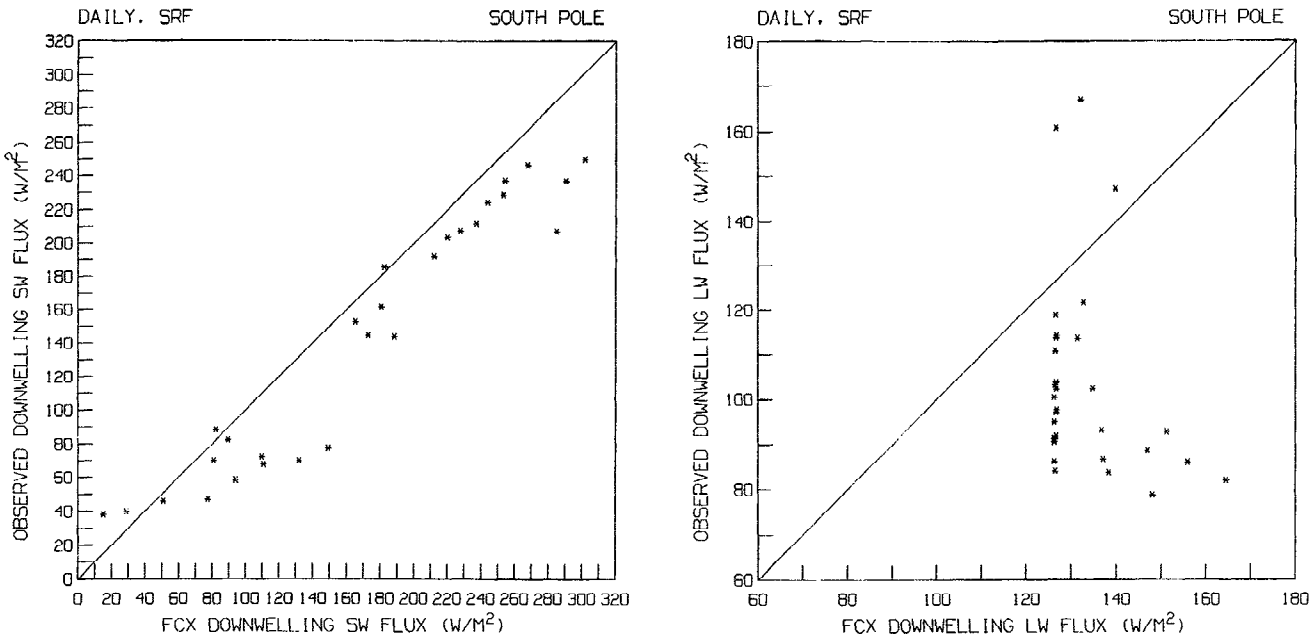

Figure 13. Same as Figure 10 but for daily mean values of (a) $S\downarrow_s$ and (b) $L\downarrow_s$ in W/m² from FCX and measured at South Pole Station.

results from the frequent use of climatological atmospheric properties over Antarctica where TOVS observations are very sparse. Thus although the magnitudes of surface flux uncertainties in polar regions are only ~ 25 W/m², they are much more significant relative to the average fluxes than at lower latitudes (see percentage differences in Tables 6 – 8).

GEBA climatology. We compare our monthly mean values of $S\downarrow_s$ and $L\downarrow_s$ from the 16 months with all data available from GEBA [*Ohmura and Gilgen,* 1991], where each surface site is matched with a single map grid cell. In most cases, there is only one station within a map grid cell, but when more than one station is available, we use the average fluxes. Hence we have only 2656 samples of $S\downarrow_s$ and 62 samples of $L\downarrow_s$ for 16 months, representing about 160 and 4 different map grid cells, respectively. The much larger number of sites reporting measurements of $S\downarrow_s$ in the GEBA database is reduced because many of these are located near each other. Figure 14 shows the comparisons of the monthly mean values of $S\downarrow_s$ and $L\downarrow_s$ and Table 9 summarizes the comparison statistics. The correlation of the two sets of $S\downarrow_s$ is 0.96; the mean and normal deviation of the differences are 15.2 and 15.7 W/m², respectively. For $L\downarrow_s$, the correlation of the two data sets is 0.84 with the mean and normal deviation of the differences equal to -19.4 and 13.4 W/m², respectively.

The normal deviations of the differences between FC and surface

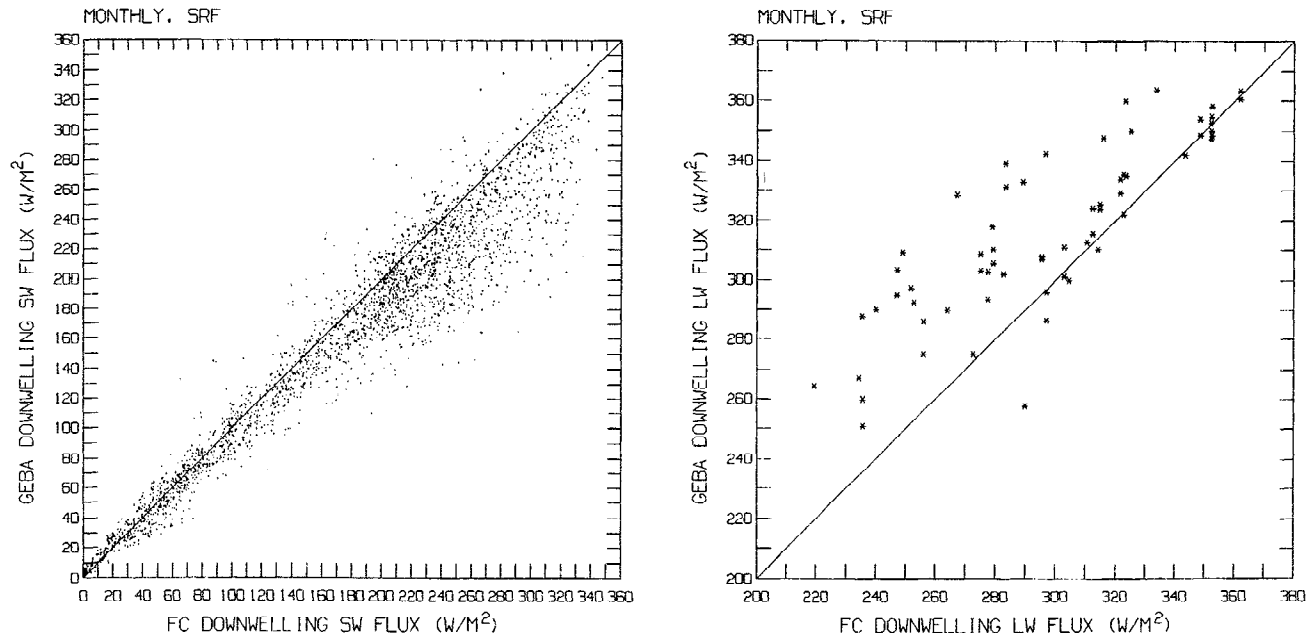

Figure 14. Same as Figure 10 but for monthly mean values of (a) $S\downarrow_s$ and (b) $L\downarrow_s$ in W/m² for FC results (abscissa) for specific locations matched to values from the Global Energy Balance Archive (GEBA) (ordinate).

Table 9. Same as Table 6 But Comparing Monthly Mean FC Values of $S\downarrow_s$ and $L\downarrow_s$ With Values Obtained From the GEBA Climatology of Surface Measurements for January, April, July and October 1985, 1986, 1987, and 1988

	$S\downarrow_s$	$L\downarrow_s$
Mean difference	15.16	-19.38
Mean difference, %	8.6	-6.5
Standard deviation	23.70	20.76
Correlation coefficient	0.9647	0.8389
Slope	0.871	0.648
Interception	7.65	123.99
Normal deviation	15.72	13.35
Normal deviation, %	8.9	4.5
Number of points	2656	62

GEBA is the Global Energy Balance Archive. Differences are for FC minus GEBA. Percentage differences are with respect to the average FCX fluxes.

site monthly mean values of $S\downarrow_s$ and $L\downarrow_s$ are similar in magnitude to the differences between daily, area-averaged values from the Wisconsin experiment. This scatter may result from comparing a large-area value with a specific point value. For $S\downarrow_s$ there are 790 map grid cells that contain at least two surface sites. Collecting the maximum and minimum differences (if there are only two sites, the maximum and minimum differences are equal) from all multisite cells, we find that the differences range from 20.0 ± 21.7 W/m² to 10.0 ± 12.7 W/m². The sensitivity of the average differences and normal deviations to the number of samples in an area suggests that both the bias and the quasi-random component of the differences in SW fluxes are significantly affected by the geographic and area mismatches between the FC data and the surface site measurements. Thus the actual uncertainty (excluding other factors producing biases) of area-averaged, monthly mean FC values of $S\downarrow_s$ and $L\downarrow_s$ is probably $\lesssim 10$ W/m², based on the Wisconsin case study.

We sort the GEBA SW comparisons (there are not enough LW surface measurements to perform this study) by the average values of the physical parameters: (1) surface temperature, visible reflectance, and total albedo; (2) cloud optical thickness, top temperature, and amount; (3) column precipitable water and ozone amount; and (4) solar zenith angle and latitude. The SW flux differences appear to be correlated with almost all parameters, including surface temperature; however, the major reason for these correlations is that the differences in $S\downarrow_s$ vary systematically with solar zenith angle, which varies with latitude, and the other parameters also vary strongly with latitude. Similarly, this relation, together with the concentration of GEBA sites in the northern hemisphere (on land), explains the large seasonal variation in the SW flux differences: the more extreme outliers (FC values below the line) in Figure 14a are associated with the summer season at the surface sites. The systematic bias in the FC values of $S\downarrow_s$ has been found by others [e.g., *Stuhlmann et al.*, 1990] but is somewhat larger in magnitude than the systematic difference of the spectral coverage between surface instruments and our calculations. The spectral effect would explain why the discrepancy is larger in proportion to the mean SW flux (which varies strongly with latitude) and why the differences are smaller whenever average cloud cover or mean optical thickness is larger (both of these effects explain a regression slope < 1). However, this discrepancy may be confused by systematic errors in aerosol optical thicknesses assumed in these calculations. We interpret the difference statistics shown in Table 9 to represent upper limits on the uncertainties in our monthly mean surface fluxes.

The comparison of FC values of $L\downarrow_s$ with the GEBA climatology shows a persistent low bias in our values (Figure 14b) that seems to increase as fluxes decrease, but the case studies show both positive and negative biases. The number of sites available for comparison of LW fluxes is too small to draw any general conclusion about the cause of this bias in our values of $L\downarrow_s$.

Other satellite-based values of $S\downarrow_s$. Table 10 compares our values of $S\downarrow_s$ with those obtained by several other authors using the same ISCCP satellite radiances, together with different subsets of parameters from the ISCCP cloud analysis. The methods employed by *Stuhlmann et al.* [1990] and *Darnell et al.* [1992] use only the observed visible radiances (although the latter method also uses the cloud amount determined by ISCCP), together with a parameterized radiative transfer model to determine $S\downarrow_s$. Monthly mean values from these two schemes generally agree with our calculations to within < 12 W/m². The *Bishop and Rossow* [1991] method uses all of the parameters determined by the ISCCP analysis (cloud amount and optical thickness as well as the surface and atmospheric properties) to determine the daily mean atmospheric transmission of SW radiation with a computationally fast parameterization based on *Frouin et al.* [1989]. This scheme was also compared with other climatologies over oceans and with the Wisconsin experiment results [*Bishop and Rossow*, 1991]. These two schemes agree to within 6 and 10 W/m² over ocean and land, respectively, for *daily* mean values. *Pinker and Laszlo* [1992] follow a similar procedure as

Table 10. Same as Table 6 But Comparing FC Values of $S\downarrow_s$ With Other Values Derived From the Same ISCCP Satellite Radiances or Cloud Products

	S & R	B & R	Pinker	Staylor
Mean difference	11.41	-0.46	0.44	4.50
Standard deviation	16.31	12.24	15.87	12.73
Correlation coefficient	0.9865	0.9923	0.9806	0.9911
Slope	0.883	1.013	0.949	0.932
Interception	12.18	-1.99	9.93	8.60
Normal deviation	9.59	8.55	11.03	8.15
Number of points	11371	6372	6241	6596

Comparisons of monthly mean values are shown for *Stuhlmann et al.* [1990] for April 1985, July 1985, October 1985, and January 1986 and for *Pinker and Laszlo* [1992] and Staylor [see *Darnell et al.*, 1992] for 10 months (April 1985, 1986, 1987, July 1985, 1986, 1987, October 1985, 1986, and January 1986, 1987). Comparisons of daily mean values are shown from *Bishop and Rossow* [1991] for 6 days in July 1986. All values are mapped to our 2.5° equal-area map and all differences are for FC minus other values.

ours, using a more detailed radiative transfer model, but they use different sources of information for most parameters. Monthly mean values from this method agree with our calculations to within 11 W/m².

4. Results

Tables 11 and 12 summarize the seasonal and annual, global mean fluxes and net fluxes obtained from this study. Seasons are represented by the averages of four examples of January (1986-1989), April (1985-1988), July (1985-1988), and October (1985-1988) conditions. Annual means are approximated by the average of the four seasonal means. The accuracy of this approximation is verified by comparing the 4-month and 12-month global mean fluxes from ERBE: average full-sky and clear-sky fluxes differ by < 0.5 W/m² and albedos differ by < 0.002. All of the TOA fluxes in these tables are spatially complete, in contrast to the values shown in Table 3 when comparing with ERBE values. The global, annual mean radiation imbalance of Earth in FC is only -4.1 W/m², apparently because our calculated planetary albedo is about 1% too high (based on the expectation that $N_t \approx 0$ or slightly positive and that NL_t is more accurate than NS_t). The total planetary albedo (not shown) is a little less than twice the clear sky value and the total LW emission is only about 8% smaller than the clear sky value. The ranges of seasonal global mean values of NS_t and NL_t are 10.0 and 7.2 W/m², respectively. *Harrison et al.* [1990] report seasonal ranges for global mean values of NS_t and NL_t from ERBE of 8.8 and 5.6 W/m², respectively. There is similar good agreement between FC and ERBE for the seasonal range of global mean clear-sky net fluxes. The largest monthly mean, global net imbalance at TOA occurs in July with a net cooling of almost 14 W/m².

The radiation balance at the surface is a net heating of about 120 W/m² and the radiation balance of the atmosphere is a net cooling of about 120 W/m². About 70% of the total SW energy absorbed by Earth (about 230 W/m²) is absorbed at the surface and about 70% of that energy is transferred from the surface to the atmosphere by nonradiative processes (primarily latent heat exchanges [*Peixoto and Oort*, 1989]). The annual variation of the global mean NS_s is about 8 W/m² and tracks that of NS_t closely; but NL_s varies only by about 5 W/m² between extremes in April and October, rather than the extremes of NL_t in January and July. The largest seasonal imbalance in the global surface radiation balance occurs in January with a net heating of about 124 W/m².

The total absorption of sunlight in the atmosphere varies by < 2 W/m² over the year, but the net emission of LW varies by about 10 W/m². The largest seasonal imbalance occurs in July with a net cooling of 129 W/m². The overall changes in N_t and N_s produced by clouds are both about -30 W/m², where the average cloud change of NS_t and NS_s (about -50 W/m²) is more than double the change of NL_t and NL_s (about 20 W/m²) (see Table 12). The average change of the global, annual mean atmospheric radiation balance caused by clouds is a small (< 6 W/m²) cooling, predominantly a change in NL_a (≈ -4 W/m², 2% of the total emission), whereas the change in NS_a is ≈ -2 W/m² (3% of the total absorption).

4.1. Radiation Balance at Top of Atmosphere

The global annual mean radiation balance of Earth (Table 12) results from net radiative heating between about 35°S and 35°N

Table 11. Global, Annual (Based on Average of Four Midseason Months) and Monthly Mean Radiative Fluxes at the Top of the Atmosphere and Surface for Full Sky, Clear Sky (CLR), Overcast Sky (CLD), and Cloud Flux Changes (CFC)

Quantity	January	April	July	October	Annual
$S\downarrow_t$	352.8	339.1	330.8	343.8	341.6
$S\uparrow_t$	117.7	109.4	105.8	113.1	111.5
$S\downarrow_s$	199.5	194.9	185.4	193.8	193.4
$S\uparrow_s$	30.6	29.7	25.0	28.0	28.3
$L\downarrow_t$	0.0	0.0	0.0	0.0	0.0
$L\uparrow_t$	231.6	232.9	238.7	233.8	234.2
$L\downarrow_s$	339.0	346.4	359.7	348.0	348.3
$L\uparrow_s$	383.7	395.5	404.8	392.5	394.1
CLR-$S\downarrow_t$	352.8	339.1	330.8	343.8	341.6
CLR-$S\uparrow_t$	60.0	59.1	54.0	58.1	57.8
CLR-$S\downarrow_s$	262.8	251.2	242.4	255.1	252.9
CLR-$S\uparrow_s$	37.6	37.3	31.8	35.7	35.6
CLR-$L\downarrow_t$	0.0	0.0	0.0	0.0	0.0
CLR-$L\uparrow_t$	252.5	255.1	259.6	254.8	255.5
CLR-$L\downarrow_s$	313.5	321.9	334.8	323.5	323.4
CLR-$L\uparrow_s$	383.7	395.5	404.8	392.5	394.1
CLD-$S\downarrow_t$	352.8	339.1	330.8	343.8	341.6
CLD-$S\uparrow_t$	135.5	126.0	124.2	130.1	129.0
CLD-$S\downarrow_s$	177.0	173.7	163.7	172.9	171.8
CLD-$S\uparrow_s$	26.0	25.1	21.7	24.2	24.2
CLD-$L\downarrow_t$	0.0	0.0	0.0	0.0	0.0
CLD-$L\uparrow_t$	225.2	225.7	231.8	226.9	227.4
CLD-$L\downarrow_s$	354.2	360.8	374.3	362.7	363.0
CLD-$L\uparrow_s$	383.7	395.5	404.8	392.5	394.1
CFC-$S\downarrow_t$	0.0	0.0	0.0	0.0	0.0
CFC-$S\uparrow_t$	57.6	50.4	51.8	55.0	53.7
CFC-$S\downarrow_s$	-63.3	-56.3	-56.9	-61.4	-59.5
CFC-$S\uparrow_s$	-7.0	-7.7	-6.8	-7.8	-7.3
CFC-$L\downarrow_t$	0.0	0.0	0.0	0.0	0.0
CFC-$L\uparrow_t$	-20.9	-22.2	-20.9	-21.1	-21.3
CFC-$L\downarrow_s$	25.4	24.6	25.0	24.6	24.9
CFC-$L\uparrow_s$	0.0	0.0	0.0	0.0	0.0

Table 12. Global, Annual (Based on Average of 4 Midseason Months) and Monthly Mean Net Radiative Fluxes at the Top of the Atmosphere, at the Surface, and in the Atmosphere for Full Sky, Clear Sky, Overcast Sky, and Cloud Flux Changes

Quantity	January	April	July	October	Annual
NS_t	235.1	229.7	225.0	230.7	230.1
NS_s	168.9	165.2	160.4	165.8	165.1
NS_a	66.2	64.4	64.6	64.9	65.0
NL_t	-231.6	-232.9	-238.7	-233.8	-234.2
NL_s	-44.8	-49.1	-45.0	-44.4	-45.8
NL_a	-186.8	-183.8	-193.6	-189.4	-188.4
N_t	3.5	-3.2	-13.7	-3.0	-4.1
N_s	124.2	116.1	115.4	121.4	119.2
N_a	-120.6	-119.4	-129.0	-124.4	-123.4
$CLR\text{-}NS_t$	292.8	280.0	276.8	285.8	283.8
$CLR\text{-}NS_s$	225.2	213.8	210.5	219.4	217.2
$CLR\text{-}NS_a$	67.6	66.2	66.3	66.4	66.6
$CLR\text{-}NL_t$	-252.5	-255.1	-259.6	-254.8	-255.5
$CLR\text{-}NL_s$	-70.2	-73.7	-70.0	-69.0	-70.7
$CLR\text{-}NL_a$	-182.3	-181.4	-189.6	-185.9	-184.8
$CLR\text{-}N_t$	40.2	25.0	17.2	30.9	28.3
$CLR\text{-}N_s$	155.0	140.2	140.5	150.4	146.5
$CLR\text{-}N_a$	-114.8	-115.2	-123.3	-119.5	-118.2
$CLD\text{-}NS_t$	217.3	213.1	206.6	213.7	212.7
$CLD\text{-}NS_s$	151.0	148.6	142.0	148.7	147.6
$CLD\text{-}NS_a$	66.3	64.5	64.5	65.0	65.1
$CLD\text{-}NL_t$	-225.2	-225.7	-231.8	-226.9	-227.4
$CLD\text{-}NL_s$	-29.5	-34.7	-30.4	-29.8	-31.1
$CLD\text{-}NL_a$	-195.7	-191.0	-201.3	-197.1	-196.3
$CLD\text{-}N_t$	-7.9	-12.6	-25.2	-13.2	-14.7
$CLD\text{-}N_s$	121.5	113.9	111.6	118.9	116.5
$CLD\text{-}N_a$	-129.4	-126.5	-136.8	-132.1	-131.2
$CFC\text{-}NS_t$	-57.6	-50.4	-51.8	-55.1	-53.7
$CFC\text{-}NS_s$	-56.3	-48.6	-50.1	-53.6	-52.2
$CFC\text{-}NS_a$	-1.4	-1.7	-1.7	-1.4	-1.6
$CFC\text{-}NL_t$	20.9	22.2	20.9	21.1	21.3
$CFC\text{-}NL_s$	25.4	24.6	25.0	24.6	24.9
$CFC\text{-}NL_a$	-4.5	-2.4	-4.1	-3.5	-3.6
$CFC\text{-}N_t$	-36.7	-28.2	-30.9	-34.0	-32.4
$CFC\text{-}N_s$	-30.8	-24.0	-25.2	-29.1	-27.3
$CFC\text{-}N_a$	-5.9	-4.1	-5.8	-4.9	-5.2

latitude and net radiative cooling in two high-latitude areas (Figure 15). The imbalances of net radiation in these zones arise from the feedback on the LW fluxes (temperature) by heat transports of the atmospheric and oceanic circulations, which cool lower latitudes and heat higher latitudes [*Peixoto and Oort*, 1989]. In radiative equilibrium, NL_t would equal NS_t at each latitude. The annual variations of NS_t, caused mostly by changing solar zenith angle, are several times larger at all latitudes than those of NL_t, caused mostly by changing atmospheric temperature. Latitudes between about 10° and 70° in both hemispheres switch from net radiative heating to net cooling during some portion of the year (Figure 16a shows annual extremes). Only the zone between 10°S and 12.5°N experiences net radiative heating all year, while the zones 70° – 90°S and 82.5° – 90°N experience net cooling all year. The moderation of seasonal NL_t (temperature) changes is produced by atmospheric heat transports and by clouds.

The latter effect is illustrated in Figures 16b and 16c. Figure 16b shows the annual mean and seasonal extremes of $CLR\text{-}N_t$, the total net flux at the top of the atmosphere that would occur in the absence of any clouds if the atmosphere and surface properties are unchanged. The seasonal change is much larger than shown in Figure 16a. The peak values of $CLR\text{-}N_t$ in the summer hemispheres are larger and occur near 60° latitude instead of 35° latitude where N_t is a maximum. Peak cooling, near 60° – 70° in the winter hemispheres is reduced slightly in magnitude. An intriguing feature is that a cloud-free Arctic would experience a brief summertime period of net radiative heating because melting sea ice has a much lower albedo than the ice sheet covering Antarctica. Figure 16c shows the difference between the values shown in Figures 16a and 16b, which we refer to as the cloud flux change, CFC. The generally lower values of this difference in summer versus winter show that the annual variation of N_t in a cloudy atmosphere is smaller than in the same atmosphere without clouds.

In the annual mean the net radiative heating at TOA over low-latitude land areas is generally 20 – 60 W/m² less than that over oceans at the same latitudes, but at higher latitudes the net radiative cooling at TOA over land is 10 – 40 W/m² larger than over oceans. In the winter hemisphere the cooling of the land areas relative to the ocean is decreased in the subtropics and increased in mid-latitudes. Figure 17 shows that clouds decrease and even reverse the land-ocean contrasts of N_t at most latitudes, except near the equator where they reinforce the contrasts [cf. *Stephens and Greenwald*, 1991b].

The quantity we call "cloud flux change" has been called "cloud radiative forcing" by a number of authors [*Ramanathan et al.*, 1989; *Harrison et al.*, 1990; *Ardanuy et al.*, 1991; *Cess et al.*, 1992];

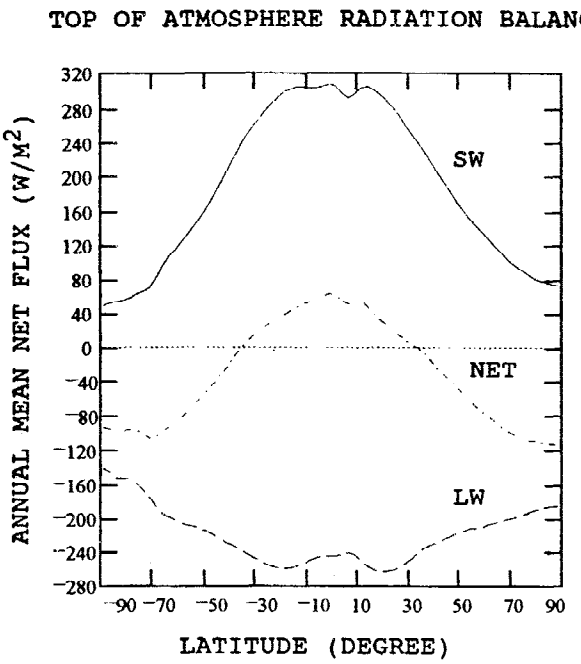

Figure 15. Annual, zonal mean FC values of (a) net SW (solid line), net LW (dashed line), and total net (dashed-dotted line) radiative fluxes at top of the atmosphere in W/m². All quantities are averaged over the mid-seasonal months in 4 years.

however, this name is misleading in three respects. Firstly, the quantity as calculated also depends on the properties of the atmosphere and surface that determine the clear sky fluxes. Four examples of significant changes in the "cloud forcing" caused by noncloud factors are as follows: (1) Since cloud properties only determine the fraction of sunlight reflected, transmitted and absorbed, daily and seasonal changes of the solar zenith angle change $S\downarrow_t$, $S\uparrow_t$ and CLR-$S\uparrow_t$ *proportionately*. (Note also that the albedo of a cloud with constant properties varies systematically with solar zenith angle because its scattering of sunlight is highly anisotropic.) Hence ($S\uparrow_t$ – CLR-$S\uparrow_t$) changes with solar zenith angle, even if cloud properties are constant. (2) Seasonal changes in the surface albedo (vegetation color changes or varying snow and ice cover) change CLR-$S\uparrow_t$. (3) Daily and seasonal changes of surface temperature alter CLR-$L\uparrow_t$, especially over land at higher latitudes. (4) Seasonal changes of atmospheric temperature and water vapor alter CLR-$L\uparrow_t$ and $L\uparrow_t$ by different amounts, depending on cloud top altitude. Hence discussions of changes in "cloud forcing" in terms of cloud feedbacks are incorrect because this quantity can vary even if clouds do not change.

Secondly, the quantity as calculated is not a forcing for anything because NS_t and NL_t refer to different volumes. Although the net radiative flux at the top of the atmosphere does represent the net balance of energy input and output for the *whole* Earth, this quantity does not indicate where the energy is deposited within the system. The equations of motion for the atmospheric and oceanic circulations [e.g., *Lorenz,* 1967] include only the net radiative heating/cooling *rate per unit volume* with units of J/m³/s or W/m³; "cloud forcing" has units of watts per meter square. Thus the *forcing* for atmospheric or oceanic circulations depends on the net flux into and out of the same volume, i.e., on the spatial distribution of the net radiative fluxes.

As we can see in Table 12, the majority of the absorbed sunlight ($NS_t = S\downarrow_t - S\uparrow_t$) is deposited at Earth's surface, while the majority of $NL_t = -L\uparrow_t$ comes from the atmosphere, not the surface. A change in NS_t that happens to be balanced by a change in NL_t (= zero "cloud forcing") actually represents a significant change in the vertical distribution of the radiative heating and cooling that drives the atmospheric circulation [cf. *Webster and Stephens,* 1984]. Hence to isolate the radiative "forcing" for the atmospheric circulation, for example, we must subtract N_s from N_t and divide by the thickness of the atmospheric layer in which the energy is deposited. Likewise, the radiative "forcing" for the ocean is given by N_s (not N_t) and the depth over which this energy is distributed.

Thirdly, the *observed* fluxes cannot be treated strictly as forcing because they already include the partial effects of the system's response in the form of the circulation feedbacks on the temperature field and hence the LW fluxes. For these reasons, "cloud forcing," as defined, neither isolates strictly cloudy effects on the TOA fluxes nor refers to a true forcing of atmospheric or oceanic circulations. We refer to this quantity as the cloud flux change, CFC, because it represents only the change in fluxes produced by adding clouds with other parameters unchanged.

The global annual mean value of CFC-N_t derived in our work is -32.4 W/m² (Table 12). Various values have been inferred from the Nimbus 7 and ERBE measurements: -17.0 and -16.6 W/m² from Nimbus 7 and ERBE, respectively [*Stephens and Greenwald,* 1991b], -26.8 W/m² from Nimbus 7 [*Ardanuy et al.,* 1991], -17.3 W/m² from ERBE [*Harrison et al.,* 1990], and -2.1 W/m² from Nimbus 7 [*Sohn and Smith,* 1992]. The difference between FC and ERBE values of CFC-N_t (matched spatial coverage from Table 3) is -15.1 W/m² and is produced about equally by the differences between values of CLR-NL_t (-9.2 W/m²) and values of NS_t (-10.5 W/m²), partially offset by the difference between the CLR-NS_t (-3.9 W/m²).

4.2. Radiation Balance at Surface

The annual mean net radiative balance at the surface is heating everywhere except over the high Antarctic plateau. The balance results from a large SW heating that is opposed by a small LW cooling: Figure 18 shows the zonal annual mean balance. NS_s/NS_t = 71.7%, indicating that about 70% of the total SW absorbed by Earth is absorbed at the surface and 30% in the atmosphere, whereas NL_s/NL_t = 19.6%, indicating that surface cooling by radiation is very inefficient. Note that NL_s is much smaller than NL_t, even though the surface temperature is much higher than the average effective atmospheric temperature. This is the atmospheric greenhouse effect: because of significant atmospheric opacity (due to water vapor and, secondarily, to clouds) $L\downarrow_s$ is nearly as large as $L\uparrow_s$ (Table 11).

Comparing the global mean FC fluxes and net fluxes from Tables 11 and 12 to those calculated by *Darnell et al.* [1992] shows generally excellent agreement (within 1 W/m²) for the magnitude of annual variations; however, there are small systematic differences (Table 13). The annual, global mean FC value of $S\downarrow_s$ is about 20 W/m² larger than reported by *Darnell et al.* [1992]; however, the cloud transmittance in their method is derived from the ISCCP visible reflectances, which for the years they consider are probably biased too high by about 6% [*Klein and Hartmann,* 1993] relative to the ISCCP data we use. This would lower their values relative to ours by at least 10 W/m². Since a calibration change alters the cloudy-sky reflectivity more than the clear-sky reflectivity, it would also cause a change in NS_s. The zonal monthly mean NL_s values agree to within about 5 W/m².

Figure 19a shows the annual, January and July zonal mean net radiation, N_s, at the surface. The large seasonal changes are caused

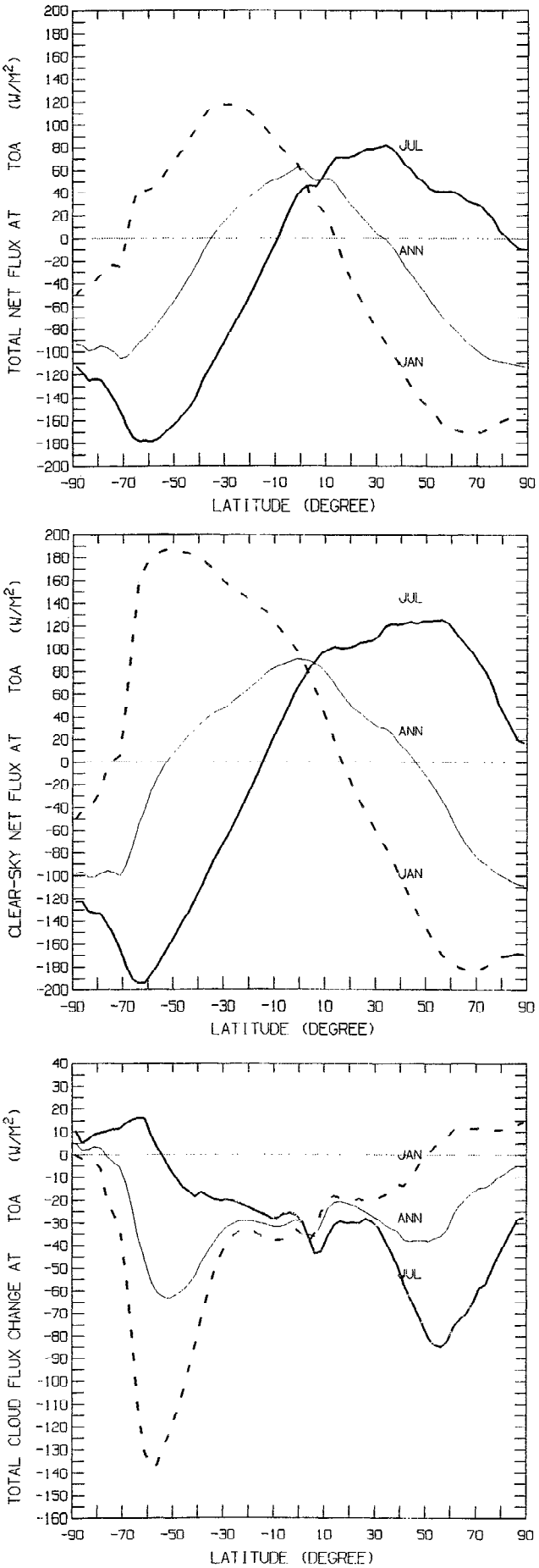

almost entirely by changing NS_s associated with solar zenith angle variation; seasonal changes in zonal mean NL_s are < 20 W/m² despite large changes in surface temperature and $L\uparrow_s$, particularly over land, because the seasonal changes in atmospheric temperature and humidity produce offsetting changes in $L\downarrow_s$ [cf. *Darnell et al.*, 1992]. Seasonal changes in hemispheric mean surface albedo are largest in the southern hemisphere because of changing illumination of Antarctica, but this only accounts for a decrease of the winter to summer change of hemispheric mean NS_s of about 10 W/m². The peak radiative heating occurs in a latitude zone from about 10° to 30° in the summer hemisphere and the winter hemisphere exhibits net radiative cooling poleward of about 50° latitude. Note that the Arctic undergoes weak net radiative heating at the surface in summer but that the surface of the Antarctic plateau still shows a small net radiative cooling even in summer.

The net radiation under clear conditions (Figure 19b) shows both a much broader latitude zone of peak summer heating, from about 10° to 60°, and an extension of the winter net cooling zone to somewhat lower latitudes, about 40°. The strong hemispheric asymmetry of peak summer radiative heating is caused both by the smaller Sun-Earth distance in January and the generally lower surface albedo at midlatitudes in the predominantly ocean-covered southern hemisphere. Land-ocean albedo differences also decrease NS_s over land with respect to oceans at the same latitude; in summer this cooling effect is reinforced by lower NL_s (more cooling) over land than oceans. In winter, the land albedo is even higher relative to ocean, because of snow cover, decreasing NS_s still further, but this is more than offset by NL_s that is also much higher (less cooling). The very strong asymmetry of summer N_s between the poles is caused by the much higher summer surface albedo of the Antarctic ice sheet compared with the melting Arctic sea ice.

Comparing Figures 19a and 19b shows that clouds not only significantly reduce the peak summer radiative heating of the surface but also shift the poleward edge of the peak heating zone equatorward by about 30° of latitude. At the same time, clouds reduce the wintertime radiative cooling at the surface at higher latitudes and shift the equatorward edge of the cooling zone toward the pole by about 10° of latitude. The pattern of zonal mean cloud flux change shows the major cloud zones and their seasonal shifts more clearly (Figure 19c). The cloud change of N_s is primarily a SW flux change resulting in a decrease of N_s relative to clear conditions in summer, but the weaker LW effects play a more important role in the high latitudes of the winter hemisphere, causing an increase of N_s relative to clear conditions in winter (Figure 19c).

Values of N_s on the land surfaces are generally less than that of the oceans and the contrast is larger in winter than summer. Figure 20 shows that the clouds act to reduce the land-ocean differences of N_s relative to clear conditions, except in the tropics (also noted by *Stephens and Greenwald* [1991b] for TOA fluxes). The extreme cloud change at 70° S in July is probably not significant because there is very little land at this latitude.

The primary process that balances the net radiative heating of the surface is evaporation (sensible heat exchanges are generally small, although more important over the drier land). Figure 21 compares the estimated annual, zonal mean surface evaporative

Figure 16. Annual (thin solid lines), January (dashed lines), and July (thick solid lines) zonal mean FC values of (a) full-sky net radiative fluxes, (b) clear -ky net fluxes, and (c) cloud changes of net fluxes in W/m² at the top of the atmosphere as functions of latitude. All quantities are averaged over the mid-seasonal months in 4 years.

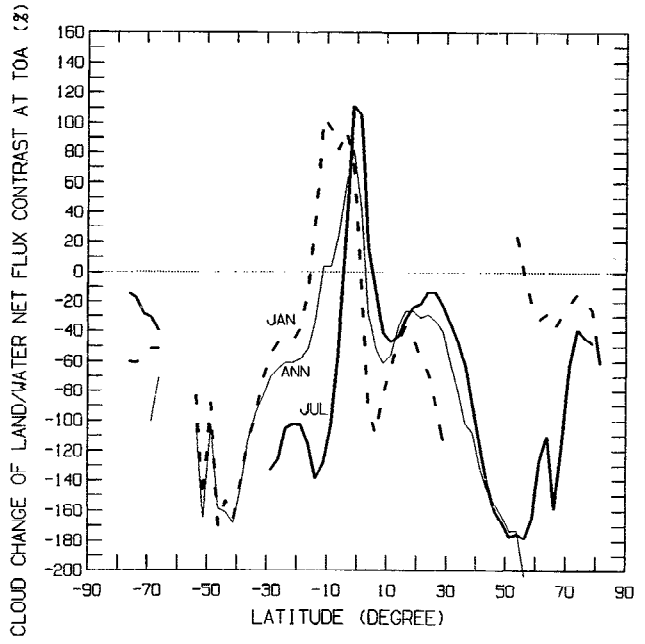

Figure 17. Cloud changes of land-water contrasts of total net radiative flux at top of atmosphere for annual (thin solid line), January (dashed line), and July (thick solid line) shown as fraction (percent) of total radiative flux contrast. Positive values indicate that clouds increase the contrast; negative values indicate that clouds decrease the contrast.

cooling [from *Peixoto and Oort,* 1989] with our calculated net surface radiative heating (full sky and clear sky). The large difference between N_s and evaporative flux near the equator, which has been decreased by clouds, implies a net heating of the tropical surface that must be balanced by ocean heat transports to higher latitudes.

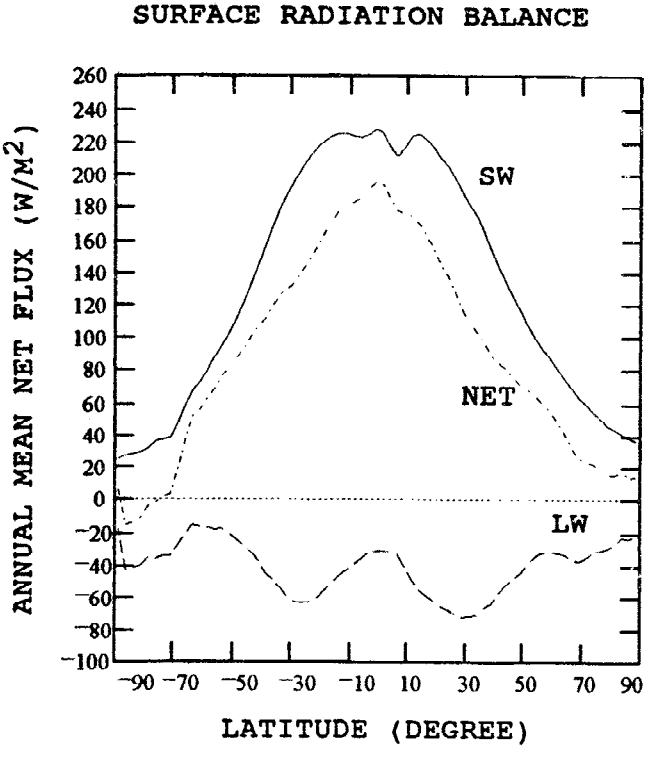

Figure 18. Same as Figure 15 but at the surface.

Table 13. Comparison of Annual Mean Surface Fluxes and Net Fluxes in Watts Per Meter Square Derived From ISCCP Data Sets by *Darnell et al.* [1992], Averaged Over July 1983, October 1983, January 1984, and April 1984, and From FC Averaged Over 4 Years

	Annual Mean		Seasonal Range	
Quantity	FC	Darnell	FC	Darnell
$S\downarrow_s$	193.4	173	14.1	12
$S\uparrow_s$	28.3	22	5.6	4
NS_s	165.1	151	8.5	4
$L\downarrow_s$	348.3	344	20.7	22
$L\uparrow_s$	394.1	389	21.1	22
NL_s	-45.8	-46	4.7	1
N_s	119.2	105	8.8	8

Notable hemispheric asymmetry and land-ocean differences of N_s are associated with the different proportions of land and ocean: lower ocean albedos result in more SW heating balanced by more efficient evaporative cooling in the southern hemisphere, whereas higher albedos and larger temperature variations over land reduce net heating balanced by less efficient evaporative cooling in the northern hemisphere (Figure 21). Clouds decrease N_s at lower latitudes relatively more than at higher latitudes (see Figure 19c), slightly decreasing the forcing for the mean oceanic circulation.

The strength of the greenhouse effect is commonly evaluated by $L\uparrow_s/L\uparrow_t$ (or the inverse), suggesting a kind of attenuation of the surface LW emission by the atmosphere [e.g., *Raval and Ramanathan,* 1989; *Stephens and Greenwald,* 1991a]. However, this quantity is not the *surface net* LW flux (the greenhouse effect is an effect on the surface net LW flux) because it completely neglects changes in $L\downarrow_s$. In particular, this quantity exaggerates the importance of changes in high-level clouds that alter $L\uparrow_t$ much more than they alter $L\downarrow_s$ and NL_s and it depends on the upper atmospheric temperature and humidity distribution much more than on the near-surface temperature and humidity [*Stephens and Greenwald,* 1991]. Moreover, *observed* LW fluxes cannot be used to evaluate the strength of a purely radiative "greenhouse" feedback [cf. *Raval and Ramanathan,* 1989] because these fluxes are significantly affected by latent heat exchanges: evaporative cooling of the surface decreases $L\uparrow_s$ and precipitation heating of the atmosphere increases $L\downarrow_s$, though not necessarily at the same place. This additional feedback is controlled by the large scale and convective motions in the atmosphere and makes the efficiency of the greenhouse effect appear larger by reducing NL_s, especially in the tropics. The more rapid decrease of $L\uparrow_s/L\uparrow_t$ near the equator (called a "supergreenhouse effect" by *Raval and Ramanathan,* [1989]) is actually a consequence of the large-scale tropical circulation that distorts (in fact exaggerates) the radiative effect by altering the vertical distributions of temperature, humidity, and clouds. Thus feedbacks on the net radiative balance *at the surface* are inextricably linked with latent (and sensible) energy exchanges.

4.3. Radiation Balance of Atmosphere

The unique aspect of our calculations is that we can separate the surface net radiation balance from the balance at the top of the atmosphere to isolate the net balance of the atmosphere in a manner that is physically consistent with the input parameter values. Even though we calculate flux divergence profiles in the model, we do not consider the vertical distribution of the atmospheric net radiation now because we have used area-averaged cloud properties assigned to a single layer. Rather we emphasize the balance of the atmosphere

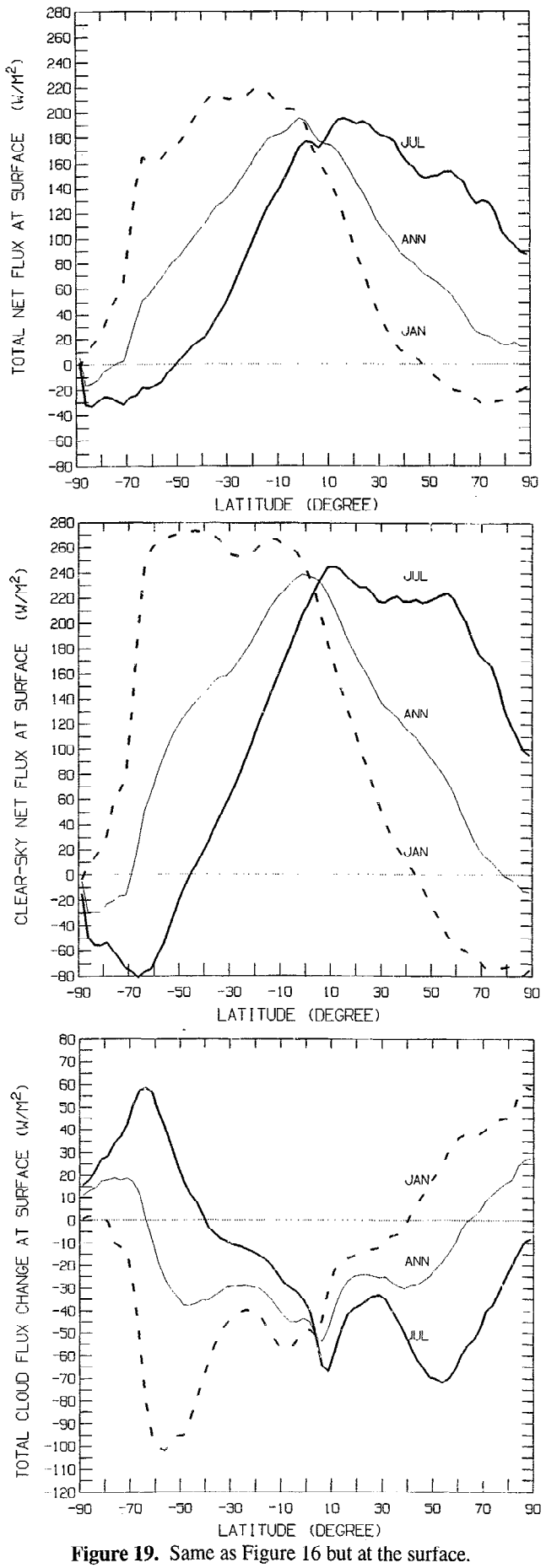

Figure 19. Same as Figure 16 but at the surface.

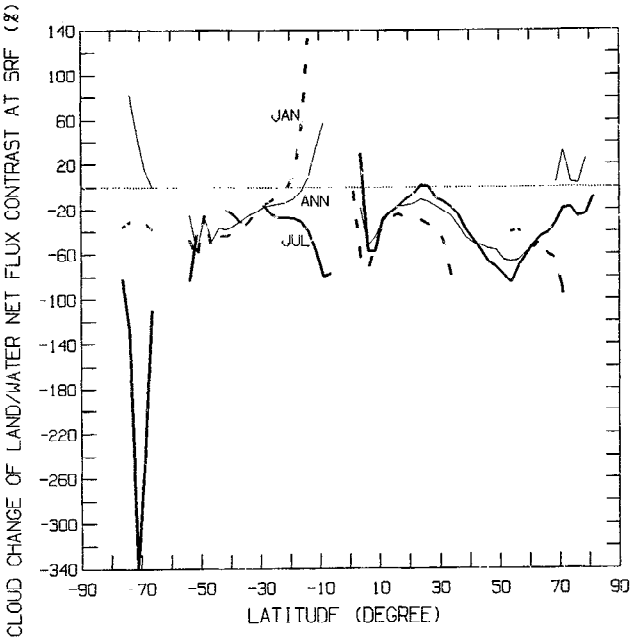

Figure 20. Same as Figure 17 but at the surface.

as a whole. We consider the net atmospheric balance to apply primarily to the troposphere: calculations indicate that about 25% (about 16 W/m²) of the total sunlight absorbed by the atmosphere (65 W/m²) is absorbed in the stratosphere, whereas only about 8% (about 19 W/m²) of the total emitted LW flux (234 W/m²) arises from the stratosphere.

The annual mean net radiative balance of the atmosphere is a nearly uniform cooling everywhere (Figure 22); the cooling over the high Antarctic plateau is much less because of generally lower temperatures and less atmospheric mass. Complementing the surface radiation balance, the atmospheric balance is primarily a large LW cooling offset by a small, very uniform SW heating. The latitudinal variations of the SW heating shows no evidence of an effect of variations of cloud properties with latitude, while the LW cooling exhibits a slightly weaker cooling near 30° – 40° in each hemisphere that is associated with a decrease of high-level cloudiness in this zone relative to other zones. The approximate latitudinal uniformity of the atmospheric radiative balance is remarkable because there are strong latitudinal gradients in atmospheric temperature, water vapor abundance, cloud amount, cloud height, and optical thickness (not shown). The lack of latitudinal variation in N_a suggests that the energy balance of the atmosphere is dominated by the heat transports of the atmospheric circulation that feedback strongly on the temperatures and, consequently, the LW cooling. Hence our evaluation of the factors controlling the atmospheric radiation balance using observations will be distorted by the effects of the atmospheric circulation on the LW fluxes.

The seasonal variations of N_a (Figure 23a) track variations in atmospheric temperature, exhibiting little variation near the equator and progressively larger changes toward the poles. The summer hemisphere experiences a net cooling that is a little more than half that of the winter hemisphere, despite much larger temperatures in summer, because of seasonal changes of SW absorption. In the absence of clouds the net cooling of the atmosphere is stronger near the equator and weaker at higher latitudes (Figure 23b). Despite a weaker seasonal cycle of temperature, the seasonal variations of CLR-N_a are larger in the southern hemisphere than in the northern hemisphere, but this difference is reduced by clouds (compare

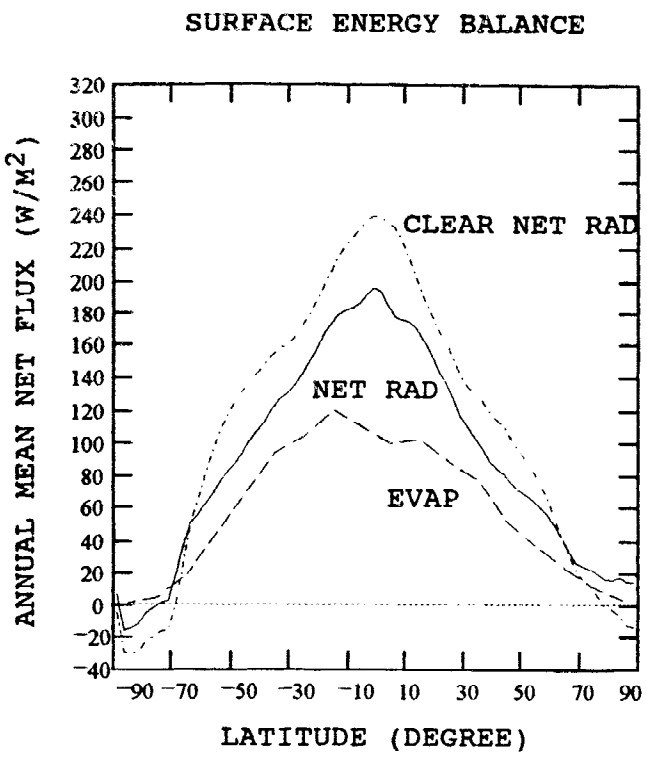

Figure 21. Annual, zonal mean surface net radiative heating for full sky and clear sky from FC and surface evaporative cooling (shown with positive sign) from *Peixoto and Oort* [1989] in W/m².

Figures 23a and 23b). A notable feature is that CLR-N_a (cooling) is nearly as strong at southern midlatitudes in winter as at the equator.

These hemispheric differences are associated with the differences in land-ocean coverage. There is little contrast in the tropical radiative cooling between land and oceans, reflecting the uniformity of atmospheric temperatures, although the atmospheric cooling is slightly stronger over the land outside of the cloudy zone. In midlatitudes on the other hand, the annual average net radiative cooling of the atmosphere is about 25% weaker over land than over oceans. In the winter the cooling contrast is almost 50%, most of the radiative cooling arising from the warmer oceanic atmosphere. In summer the cooling contrast nearly disappears.

The cloud changes of the net atmospheric radiation balance are very subtle: the global, annual mean value of CFC-N_a is only -5 W/m² (Table 12). The cloud change of NS_a is very weak; the global annual average difference between CLR-NS_a and CLD-NS_a is only 1.5 W/m² (Table 12). This explains the lack of features in zonal mean values of NS_a (Figure 22). However, this weak effect actually results from three larger but offsetting changes when clouds are added to the atmosphere: (1) the higher albedo of clouds increases the upwelling SW flux and the amount absorbed by water vapor above the clouds, (2) the amount of SW flux absorbed in the cloud layer increases because clouds absorb more at near-IR wavelengths than the gases and because the larger scattering optical thickness lengthens the average photon path length through the absorbing gases, and (3) clouds block a large fraction of the SW flux that would be absorbed by the water vapor below. The first two effects increase the total SW absorption in the atmosphere by an amount that decreases as cloud altitude increases. The third effect decreases the total SW absorption in the atmosphere by an amount that increases as cloud altitude increases. For the observed cloud vertical distribution the third effect is slightly larger than the other two because most of the water vapor (primary absorber) is below the clouds. Note that comparing SW flux measurements at TOA and surface cannot separate the cloud absorption changes from associated changes in water vapor absorption.

Thus the primary change of N_a by clouds is a LW flux change. The change in the tropics is a decrease of NL_a in the Inter Tropical Convergence Zone (ITCZ) (Figure 23c), produced primarily by decreasing the effective emission temperature. At higher latitudes, clouds increase NL_a by increasing the effective emissivity of the atmosphere in the water "window" (8 to 14 μm wavelength), even though they also lower the average emission temperature somewhat. The change of emissivity is less important in the tropics because of the much larger water vapor opacity there. Clouds slightly enhance the land-ocean contrasts of the atmospheric cooling, except in the tropics where they decrease weak contrasts (Figure 24). Comparing the latitudinal pattern of CFC-N_a (Figure 23c) with that of NL_a (Figure 22) suggests that the features in NL_a must be produced by variations in the vertical distribution of water vapor [cf. *Stephens and Greenwald,* 1991a, b], rather than by clouds. Note that if the proper spectral dependence of the radiative fluxes on cloud and water vapor changes were not included in the radiative model, e.g., by using so-called "broadband" optical properties, the latitudinal variation of CFC-NL_a might be missed.

Figure 25 compares the latitudinal distribution of both the annual mean full-sky and clear-sky net radiative cooling of the atmosphere and the distribution of precipitation (latent heating) from *Peixoto and Oort* [1989]. In the tropics, precipitation and SW heating are opposed by LW cooling, but the presence of clouds reduces the LW cooling, which is equivalent to net heating effect (Figure 23c). At midlatitudes the precipitation and SW heating and the LW cooling are all reduced, but the clouds enhance the LW cooling (Figure 23c), particularly in the winter hemisphere. Thus even though clouds reduce the total heating of Earth overall (Table 12), this cooling effect appears primarily at the surface where it would serve to decrease latent heat fluxes. The global mean cloud change of the atmospheric radiative balance is only -5 W/m², but the cloud flux

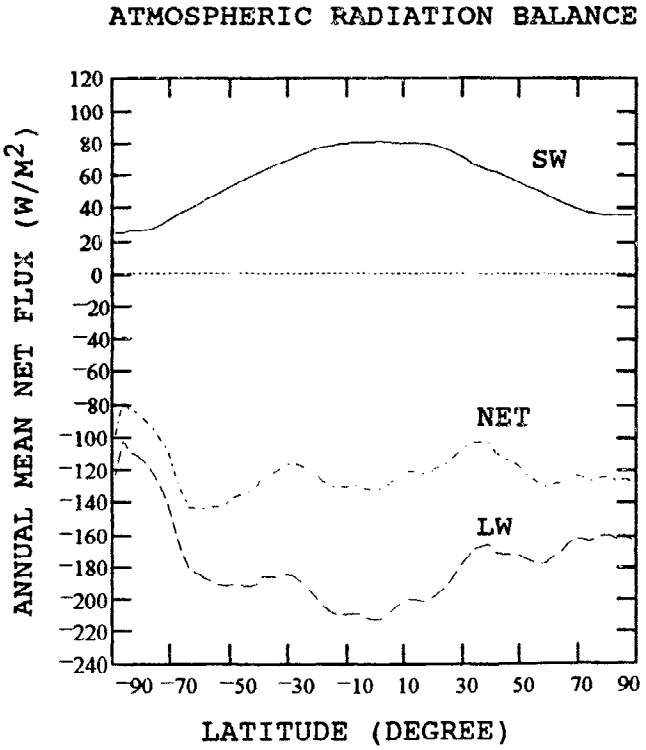

Figure 22. Same as Figure 15 but in the atmosphere.

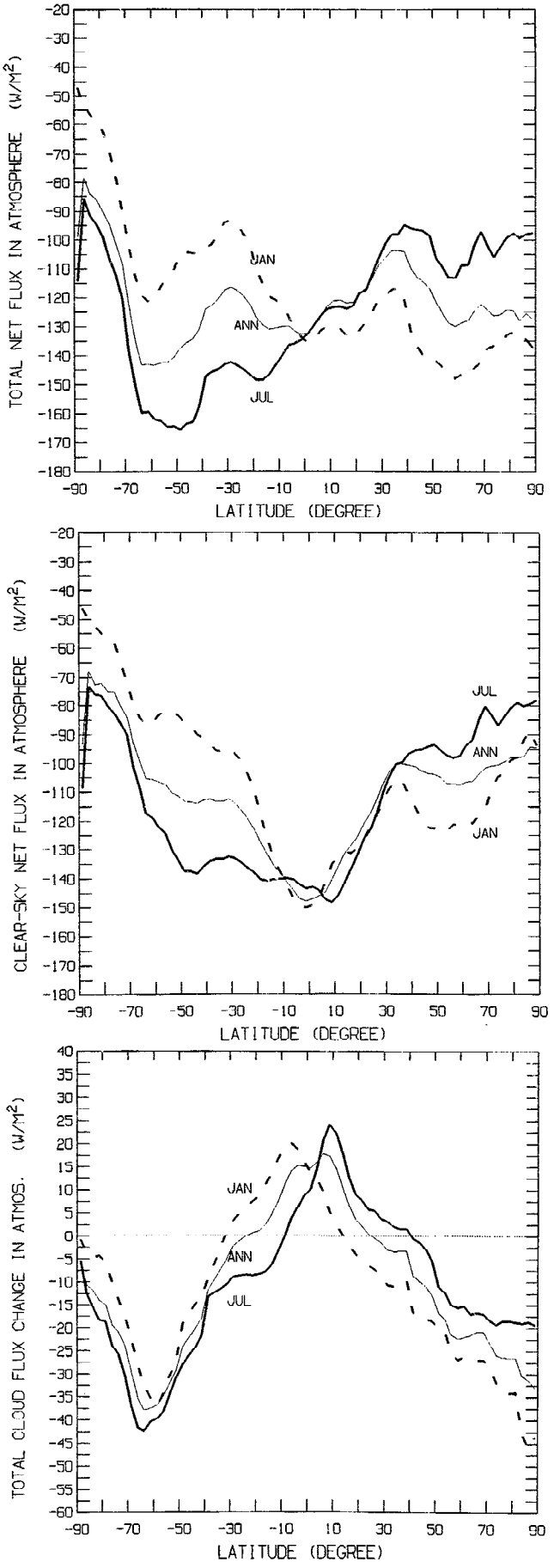

Figure 23. Same as Figure 16 but in the atmosphere.

changes alter the latitudinal gradient of the net radiative balance of the atmosphere so as to reinforce the general radiative and latent forcing for the general circulation. The clouds also enhance the land-ocean contrast which would reinforce the standing eddy component of the circulation, contrary to the conclusion reached by comparing TOA fluxes [*Stephens and Greenwald,* 1991b].

5. Summary

5.1. Validation

Our validation studies suggest that the specification of cloud effects is no longer the leading uncertainty in reconstructing the radiative fluxes at the top of atmosphere and the surface, but rather cloud properties are now roughly equal contributors to the uncertainty, along with surface and atmospheric properties. Overall, the estimated uncertainties (rms) in regional, monthly mean values of $S\uparrow_t$, $L\uparrow_t$, $S\downarrow_s$, $S\uparrow_s$, $L\downarrow_s$ and $L\uparrow_s$ are as follows.

1. The bias of $S\uparrow_t$, based on comparison with ERBE, is 11 W/m² with a rms scatter of 7 W/m² (daily mean scatter is about 15 W/m²). However, judging from the estimated uncertainty of the ERBE values and the global annual mean radiation imbalance, the bias in our values could be as small as about 5 W/m². A significant contribution to the bias comes from our estimates of surface albedos, particularly over land and snow/ice, but we also note some systematic problems with ERBE angle models for some surface types [*Hartmann and Doelling,* 1991; *Suttles et al.,* 1992]. We note a systematic variation of the differences in $S\uparrow_t$ as function of cloud fraction that may be caused by differences between the ERBE scene-dependent (cloud cover dependent) angle models and the Mie scattering treatment used both for ISCCP retrievals and in our flux calculations. The latter is also affected by use of spherical water droplets and plane-parallel geometry to calculate scattering.

2. The bias of $L\uparrow_t$, based on comparison with ERBE, is -1 W/m² with a rms scatter of 4 W/m² (daily mean scatter is about 10 W/m²). The larger bias (about -9 W/m²) suggested by ERBE in clear sky cannot be explained by biases of the input atmospheric parameters because there is no evidence for such large errors (temperatures would have to change by almost 4 K or water vapor by about 60%). However, the ERBE values may be biased high by about 5 W/m² because of the scene identification procedure as reported by *Harrison et al.* [1990] and *Hartmann and Doelling* [1991]. We also note that the diurnal cycle of ERBE values of CLR-$L\uparrow_t$ over land is symmetric about noon, contrary to observations of surface temperature [e.g., *Sellers,* 1965], indicating possible problems with the ERBE models used to interpolate the sparse diurnal sampling. This problem can also contribute to a high bias in the ERBE values of CLR-$L\uparrow_t$ over land.

3. The bias of $S\downarrow_s$, based on all the case studies and the GEBA climatology, is about 10 – 15 W/m² with a rms scatter of 10 – 15 W/m² (daily mean scatter from case studies is also about 10 – 15 W/m²), depending on latitude (i.e., depending on the mean flux). Judging from the only case with an array of surface sites, the monthly mean scatter is probably < 10 W/m²; the larger scatter with GEBA is caused by comparing pointlike surface measurements with area-averaged satellite results. Part of the bias is also caused by comparison of point measurements with area-averaged values. Most of the difference occurs under clear conditions implicating factors other than clouds. At least half of the bias can be accounted for by the difference in spectral coverage between our calculations and the measurements by surface SW instruments. Some portion of the bias may be caused by an underestimate of aerosol optical thicknesses.

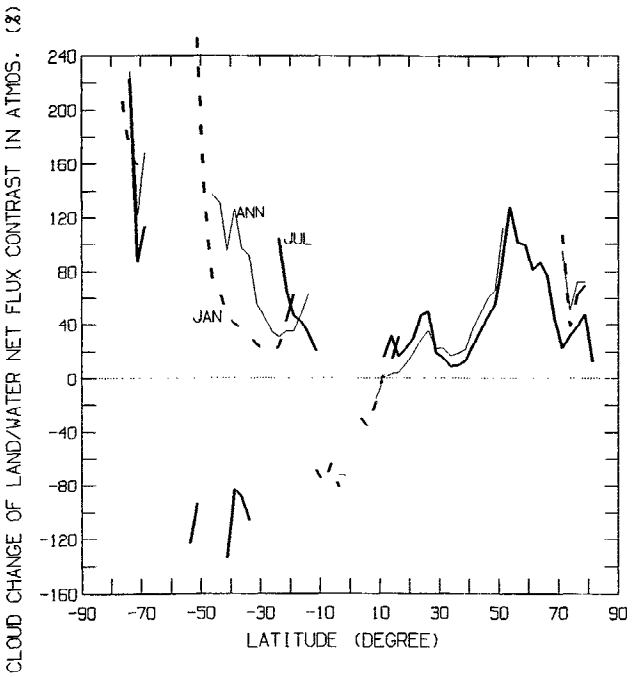

Figure 24. Same as Figure 17 but in the atmosphere.

4. The bias of $S\uparrow_s$, based on comparison with ERBE, is only ≈ 3 W/m² because surface albedos are generally very low; the corresponding high bias in surface albedos is about 0.01 over oceans and about 0.02 over land. The rms scatter is the same for monthly and daily values, about 10 W/m² (corresponding to an albedo scatter of about 0.03). Uncertainties for snow- and ice-covered surfaces are about twice as large.

5. The bias of $L\downarrow_s$, based on all the case studies and the GEBA climatology, is difficult to estimate. Tropical values may be biased high by at least 10 W/m² and higher-latitude values may be biased low by a similar amount. If uncertainty estimates for TOVS atmospheric temperatures, the dominant source of uncertainty, are accurate (± 2 K), then the bias of $L\downarrow_s$ is probably < 15 W/m² but variable in sign with location. The rms scatter of $L\downarrow_s$ is at least 15 W/m² (daily mean scatter is about the same magnitude). Uncertainties in atmospheric temperature and water vapor abundance lead to an overestimate of daily variations of $L\downarrow_s$ in the tropics, but poor time sampling leads to an underestimate at higher latitudes. Uncertainties in $L\downarrow_s$ caused by uncertainties in cloud base location are generally unimportant by comparison.

6. $L\uparrow_s$ is probably the most uncertain flux component because it is very sensitive to the effects of cloud detection errors on satellite-retrieved surface temperatures. Separating the bias and rms scatter is difficult because there are no widespread measurements of surface skin temperature or $L\uparrow_s$ to verify the satellite estimates. The best estimates of uncertainties in the ISCCP surface temperatures suggest biases $\lesssim 2$ K over oceans and $\lesssim 4$ K over land with similar rms scatter [*Rossow and Garder,* 1993]. The corresponding bias and rms scatter of $L\uparrow_s$ are $\lesssim 12$ and $\lesssim 24$ W/m², respectively. An additional source of uncertainty of $L\uparrow_s$ on land is caused by uncertain surface emissivities, which probably produce a low bias in our values of as much as 10 W/m².

5.2. Radiation Balance and the Role of Clouds

The advantage of calculating fluxes from the observed physical properties is that we can isolate each contribution and can examine the TOA, surface, and atmospheric radiation balances separately. The most notable results are as follows: (1) The net SW heating of Earth appears predominantly at the surface, whereas the net LW cooling arises predominantly from the atmosphere [cf. *Peixoto and Oort,* 1989]. Clouds generally decrease both the net SW heating and the net LW cooling of Earth, the former effect being about twice the magnitude of the latter effect, as inferred from TOA fluxes (e.g., *Harrison et al.,* [1990]; see *Hartmann et al.,* [1986] for more discussion). However, these effects appear mostly at the surface rather than *in* the atmosphere. That is, the TOA cloud flux changes are nearly the same as the surface flux changes. (2) Clouds have almost no *net* effect on the global mean amount of SW radiation absorbed by the atmosphere, but they do redistribute the absorption. Rather they enhance the latitudinal gradient in the LW cooling, thereby reinforcing the general radiative forcing for the atmospheric general circulation. This effect arises from a delicate interplay between water vapor and clouds that varies with latitude and season (at higher latitudes). Although increasing latitudinal gradients in general, clouds at the same time reduce seasonal changes in the net radiation. Both of these effects suggest that the vertical distribution of clouds will also alter the diabatic heating/cooling that forces the atmospheric circulation [*Webster and Stephens,* 1984]. (3) Clouds generally reduce the land-water contrasts of the net radiative balance at TOA and the surface but increase the contrasts in the atmosphere, which implies that cloud effects also reinforce the growth of standing eddy motions in the atmosphere.

A significant feature of this analysis is that the cloud changes of the radiative balance are relatively small in magnitude compared with the total net fluxes. This result emphasizes the importance of monitoring the variations of clouds, together with those of the surface and atmosphere, because the complex geographic variations of the properties of all three, particularly latitudinal gradients and land-ocean contrasts, preclude a precise diagnosis of the effect of clouds

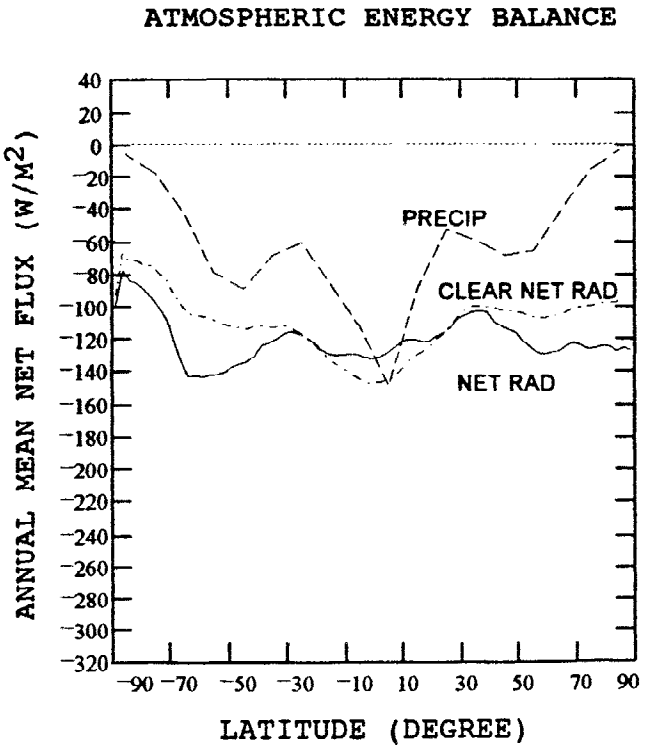

Figure 25. Annual, zonal mean atmospheric net radiative cooling for full sky and clear sky from FC and atmospheric heating by precipitation (shown with negative sign) from *Peixoto and Oort* [1989] in W/m².

on the radiation balance from the measurement of radiative fluxes alone. This result also emphasizes the need to keep working on the quality of available observations and flux calculation methods to decrease the uncertainties in the diagnosed radiative fluxes.

Acknowledgments. We thank Andy Lacis, Barbara Carlson, Carol Anne Clayson, Judy Curry, Tony DelGenio, Graeme Stephens, Peter Webster, and Tom Vonder Haar for conversations that helped us shape the interpretation of our results. This work was supported by the NASA Global Change Model-Data Assessment program under James C. Dodge in the Earth System Modeling and Global Analysis branch under Robert A. Schiffer and by NSF ATM-9110536 for participation in TOGA-COARE (J.A. Curry, PI).

References

Albrecht, B., and S. K. Cox, Procedures for improving pyrgeometer performance, *J. Appl. Meteorol., 16*, 188-197, 1977.

Ardanuy, P. E., L. L. Stowe, A. Gruber, and M. Weiss, Shortwave, longwave and net cloud-radiative forcing as determined from Nimbus 7 observations, *J. Geophys. Res., 96*, 18,537-18,549, 1991.

Bishop, J. K. B., and W. B. Rossow, Spatial and temporal variability of global surface solar irradiance, *J. Geophys. Res., 96*, 16,839-16,858, 1991.

Brooks, C. E. P., *Climate Through the Ages*, (revised), 395 pp., Dover, Mineola, N.Y., 1949.

Brooks, D. R., and P. Minnis, Comparison of longwave diurnal models applied to simulations of the Earth Radiation Budget Experiment, *J. Clim. Appl. Meteorol., 23*, 155-160, 1984a.

Brooks, D. R., and P. Minnis, Simulation of the Earth's monthly average regional radiation balance derived from satellite measurements, *J. Clim. Appl. Meteorol., 23*, 392-403, 1984b.

Brooks, D. R., E. F. Harrison, P. Minnis, J. T. Suttles, and R. S. Kandel, Development of algorithms for understanding the temporal and spatial variability of the Earth's radiation balance, *Rev. Geophys., 24*, 422-438, 1986.

Budyko, M. I., *Climate and Life*, edited by D.H. Miller, 508 pp., Academic, San Diego, Calif., 1974.

Cess, R. D., E. F. Harrison, P. Minnis, B. R. Barkstrom, V. Ramanathan, and T. Y. Kwon, Interpretation of seasonal cloud-climate interactions using Earth Radiation Budget Experiment data, *J. Geophys. Res., 97*, 7613-7617, 1992.

Charlson, R. J., J. Langner, H. Rodhe, C. B. Leovy, and S. G. Warren, Perturbation of the Northern Hemisphere radiative balance by back-scattering from anthropogenic sulfate aerosols, *Tellus, 43(AB)*, 152-163, 1991.

Cox, S. K., D. S. McDougal, D. A. Randall, and R. A. Schiffer, FIRE - the First ISCCP Regional Experiment, *Bull. Am. Meteorol. Soc., 68*, 114-118, 1987.

Darnell, W. L., W. F. Staylor, S. K. Gupta, N. A. Ritchey, and A. C. Wilber, Seasonal variation of surface radiation budget derived from International Satellite Cloud Climatology Project C1 data, *J. Geophys. Res., 97*, 15,741-15,760, 1992.

Durkee, P. A., F. Pfeil, E. Frost, and R. Shema, Global analysis of aerosol particle characteristics, *Atmos. Environ., 25A*, 2457-2471, 1991.

Dutton, E. G., R. S. Stone, D. W. Nelson, and B. G. Mendonca, Recent interannual variations in solar radiation, cloudiness and surface temperature at the south pole, *J. Clim., 4*, 848-858, 1991.

Ellis, J. S., and T.H. Vonder Haar, Zonal average earth radiation budget measurements from satellites for climate studies, *Atmos. Sci. Rep., 240,* **Colo. State Univ., Boulder, 1976.**

Frouin, R., D. W. Lingner, C. Gautier, K. S. Baker, and R. C. Smith, A simple analytical formula to compute clear sky total and photo-synthetically available solar irradiance at the ocean surface, *J. Geophys. Res., 94*, 9731-9742, 1989.

Fu, R., A. D. DelGenio, and W. B. Rossow, Behavior of deep convective clouds in the tropical Pacific deduced from ISCCP radiances, *J. Clim., 3*, 1129-1152, 1990.

Gautier, C., G. Diak, and S. Masse, A simple physical model to estimate incident solar radiation at the surface from GOES satellite data, *J. Appl. Meteorol., 19*, 1005-1012, 1980.

Hansen, J. E., and L. D. Travis, Light scattering in planetary atmospheres, *Space Sci. Rev., 16*, 527-610, 1974.

Hansen, J., G. Russell, D. Rind, P. Stone, A. Lacis, S. Lebedeff, R. Ruedy, and L. Travis, Efficient three-dimensional models for climate studies: Models I and II, *Mon. Weather Rev., 111*, 609-662, 1983.

Hansen, J., I. Fung, A. Lacis, D. Rind, S. Lebedeff, R. Ruedy, G. Russell, and P. Stone, Global climate changes as forecast by the Goddard Institute for Space Studies three-dimensional model, *J. Geophys. Res., 93*, 9341-9364, 1988.

Harrison, E. F., P. Minnis, B. R. Barkstrom, V. Ramanathan, R. D. Cess, and G. G. Gibson, Seasonal variation of cloud radiative forcing derived from the Earth Radiation Budget Experiment, *J. Geophys. Res., 95*, 18,687-18,703, 1990.

Hartmann, D. L., and D. Doelling, On the net radiative effectiveness of clouds, *J. Geophys. Res., 96*, 869-891, 1991.

Hartmann, D. L., V. Ramanathan, A. Berroir, and G. E. Hunt, Earth radiation budget data and climate research, *Rev. Geophys., 24*, 439-468, 1986.

Hartmann, D. L., K. J. Kowalewsky, and M. L. Michelsen, Diurnal variations of outgoing longwave radiation and albedo from ERBE scanner data, *J. Clim., 4*, 598-617, 1991.

Hickey, J. R., B. M. Alton, H. L. Kyle, and D. V. Hoyt, Total solar irradiance measurements by ERB/Nimbus 7, A review of nine years, *Space Sci. Rev., 48*, 321-342, 1988.

House, F. B., A. Gruber, G. E. Hunt, and A. T. Mecherikunnel, History of satellite missions and measurements of the Earth Radiation Budget (1957-1984), *Rev. Geophys., 24*, 357-378, 1986.

Husar, R. B., J. M. Holloway, D. E. Patterson, and W. E. Wilson, Spatial and temporal pattern of eastern U.S. haziness: A summary, *Atmos. Environ., 15*, 1919-1928, 1981.

Jacobowitz, H., N. L. Smith, H. B. Howell, F. W. Nagle, and J. R. Hickey, The first 18 months of planetary radiation budget measurements from the Nimbus 6 ERB experiment, *J. Atmos. Sci., 36*, 502-507, 1979.

Klein, S. A., and D. L. Hartmann, Spurious trends in the ISCCP C2 data set, *Geophys. Res. Lett., 20*, 455-458, 1993.

Kyle, H. L., A. Mecherikunnel, P. Ardanuy, L. Penn, B. Groveman, G. G. Campbell, and T. H. Vonder Haar, A comparison of two major Earth radiation budget data sets, *J. Geophys. Res., 95*, 9951-9970, 1990.

Kyle, H. L., et al., The Nimbus earth radiation budget (ERB) experiment: 1975 to 1992, *Bull. Am. Meteorol. Soc., 74*, 815-830, 1993.

Lacis, A. A., and V. Oinas, A description of the correlate k-distribution method for modeling non-grey gaseous absorption, thermal emission, and multiple scattering in vertically inhomogenous atmospheres, *J. Geophys. Res., 96*, 9027-9063, 1991.

Li, Z., H. G. Leighton, K. Masuda, and T. Takashima, Estimation of SW flux absorbed at the surface from TOA reflected flux, *J. Clim., 6*, 317-330, 1993.

London, J. R., B. D. Bojkov, S. Oltmans, and J. F. Kelly, Atlas of the Global Distribution of Total Ozone, July 1957-July 1967, *NCAR Tech. Note 113 + STR*, 276 pp., Nat. Cent. for Atmos. Res., Boulder, Colo., 1976.

Lorenz, E. N., The nature and theory of the general circulation of the atmosphere, *WMO Rep. 218.TP.115*, 161 pp., World Meteorol. Organ., Geneva, 1967.

Matthews, E., Global vegetation and land use: New high-resolution data bases for climate studies, *J. Clim. Appl. Meteorol., 22*, 474-487, 1983.

McClatchey, R. A., R. W. Fenn, J. E. A. Selby, F. E. Volz, and J. S. Garing, Optical Properties of the Atmosphere, *AFCRL-72-0497, Environ. Res. Pap., 411*, 108 pp., Air Force Cambridge Res. Labs., Hanscom Air Force Base, Mass., 1972.

McMillin, L. M., Evaluation of a classification method for retrieving atmospheric temperatures from satellite measurements, *J. Appl. Meteorol., 30*, 432-446, 1991.

Minnis, P., and E. F. Harrison, Diurnal variability of regional cloud and clear sky radiative parameters derived from GOES data, 2, November

1978 cloud distributions, *J. Clim. Appl. Meteorol., 23*, 1012-1031, 1984a.

Minnis, P., and E. F. Harrison, Diurnal variability of regional cloud and clear-sky radiative parameters derived from GOES data, 3, November 1978 radiative parameters, *J. Clim. Appl. Meteorol., 23*, 1032-1051, 1984b.

Ohmura, A., and H. Gilgen, The GEBA data base, interactive applications, retrieving data, Global Energy Balance Archive, GEBA, *World Clim. Prog. Water Proj. A7, Rep. 2*, 60 pp, Zürcher Geogr. Scrift., Zürich, Switzerland, 1991.

Ohring, G., and A. Gruber, Satellite radiation observations and climate theory, *Adv. Geophys., 25*, 237-304, 1983.

Peixoto, J. P., and A. H. Oort, *Physics of Climate*, 520 pp., American Institute of Physics, New York, 1989.

Pinker, R. T., and I. Laszlo, Modeling surface solar irradiance for satellite applications on a global scale, *J. Appl. Meteorol., 31*, 194-211, 1992.

Poore, K., J.-H. Wang, and W. B. Rossow, Climatology of cloud layer thicknesses from a combination of surface and upper air observations, in *J. Clim.*, in press, 1995.

Ramanathan, V., R. D. Cess, E. F. Harrison, P. Minnis, B. R. Barkstrom, E. Ahmad, and D. Hartmann, Cloud-radiative forcing and climate: Results from the Earth Radiation Budget Experiment, *Science, 243*, 57-63, 1989.

Raschke, E., T. H. Vonder Haar, W. R. Bandeen, and M. Pasternak, The annual radiation balance of the earth-atmosphere system during 1967-70 from Nimbus 3 measurements, *J. Atmos. Sci., 30*, 341-364, 1973.

Raval, A., and V. Ramanathan, Observational determination of the greenhouse effect, *Nature, 342*, 758-761, 1989.

Rieland, M., and E. Raschke, Diurnal variability of the earth radiation budget: Sampling requirements, time integration aspects and error estimates for the Earth Radiation Budget Experiment (ERBE), *Theor. Appl. Climatol., 44*, 9-24, 1991.

Roberts, R. E., J. E. A. Selby, and L. M. Biberman, Infrared continuum absorption by atmospheric water vapor in the 8-12 μm window, *Appl. Opt., 15*, 2085-2090, 1976.

Rossow, W. B., and L. C. Garder, Validation of ISCCP cloud detections, *J. Clim., 6*, 2370-2393, 1993.

Rossow, W. B., and A. A. Lacis, Global, seasonal cloud variations from satellite radiance measurements, 2, Cloud properties and radiative effects, *J. Clim., 3*, 1204-1253, 1990.

Rossow, W. B., and R. A. Schiffer, ISCCP cloud data products, *Bull. Am. Meteorol. Soc., 72*, 2-20, 1991.

Rossow, W. B., L. C. Garder, P. J. Lu, and A. W. Walker, International Satellite Cloud Climatology Project (ISCCP) Documentation of Cloud Data, *WMO/TD-266*, (revised), 76 pp. plus three appendices, World Clim. Res. Progr. (ICSU and WMO), Geneva, March, 1991.

Schiffer, R. A., and W. B. Rossow, ISCCP global radiance data set: A new resource for climate research, *Bull. Am. Meteorol. Soc., 66*, 1498-1505, 1985.

Sellers, W. D., *Physical Climatology*, University of Chicago, Chicago, Ill., 1965.

Sèze, G., and W. B. Rossow, Time-cumulated visible and infrared radiance histograms used as descriptors of surface and cloud variations, *Int. J. Remote Sens., 12*, 877-920, 1991a.

Sèze, G., and W. B. Rossow, Effects of satellite data resolution on measuring the space-time variations of surfaces and clouds, *Int. J. Remote Sens., 12*, 921-952, 1991b.

Simpson, G. C., The distribution of terrestrial radiation, *Mem. R. Meteorol. Soc., 3*, 53-78, 1929.

Smith, W. L., H. M. Woolf, C. M. Hayden, D. Q. Wark, and L. M. McMillin, The TIROS-N Operational Vertical Sounder, *Bull. Am. Meteorol. Soc., 60*, 117-118, 1979.

Smith, G. L., R. N. Green, E. Raschke, L. M. Avis, J. T. Suttles, B. A. Wielicki, and R. Davies, Inversion methods for satellite studies of the Earth's radiation budget: Development of algorithms for the ERBE mission, *Rev. Geophys., 24*, 407-421, 1986.

Sohn, B.-J., and E. A. Smith, The significance of cloud-radiative forcing to the general circulation on climate time scale — A satellite interpretation, *J. Atmos. Sci., 49*, 845-860, 1992.

Stephens, G. L., and T. J. Greenwald, The Earth's radiation budget and its relation to atmospheric hydrology, 1, Observations of the clear sky greenhouse effect, *J. Geophys. Res., 96*, 15,311-15,324, 1991a.

Stephens, G. L., and T. J. Greenwald, The Earth's radiation budget and its relation to atmospheric hydrology, 2, Observations of cloud effects, *J. Geophys. Res., 96*, 15,325-15,340, 1991b.

Stuhlmann, R., M. Rieland, and E. Raschke, An improvement of the IGMK model to derive total and diffuse solar-radiation at the surface from satellite data, *J. Appl. Meteorol., 29*, 586-603, 1990.

Suttles, J. T., et al., Angular Radiation Models for the Earth-Atmosphere System, vol. 1, Shortwave Radiation, in *NASA RP-1184*, 144 pp., 1988.

Suttles, J. T., R. N. Green, G. L. Smith, B. A. Wielicki, I. J. Walker, V. R. Taylor, and L. L. Stowe, Angular Radiation Models for the Earth-Atmosphere System, 2, Longwave Radiation, in *NASA RP-1184*, 84 pp., 1989.

Suttles, J. T., B. A. Wielicki, and S. Vemury, Top of atmosphere radiative fluxes: Validation of ERBE scanner inversion algorithm using Nimbus 7 ERB data, *J. Appl. Meteorol., 31*, 784-796, 1992.

Toon, O. B., and J. B. Pollack, A global average model of atmospheric aerosols for radiative transfer calculations, *J. Appl. Meteorol., 15*, 225-246, 1976.

Vonder Haar, T. H., and V. E. Suomi, Measurements of the Earth's radiation budget from satellites during a five-year period, 1, Extended time and space means, *J. Atmos. Sci., 28*, 305-314, 1971.

Webster, P. J., and G. L. Stephens, Cloud-radiation interaction and the climate problem, in *The Global Climate*, edited by J.T. Houghton, pp. 63-78, Cambridge University Press, New York, 1984.

Wetzel, P. J., D. Atlas, and R. H. Woodward, Determining soil moisture from geosynchronous satellite infrared data: A feasibility study, *J. Clim. Appl. Meteorol., 23*, 375-391, 1984.

Whitlock, C. H., et al., Comparison of surface radiation budget satellite algorithms for downwelled shortwave irradiance with Wisconsin FIRE/SRB surface-truth data, in *Proceedings of the Seventh Conference on Atmospheric Radiation, American Meteorogical Society*, pp. 237-242, Boston, Mass., 1990a.

Whitlock, C. H., J. E. Hay, D. A. Robinson, S. K. Cox, D. I. Wardle, and S. R. LeCroy, Downward shortwave surface irradiance from 17 sites for the FIRE/SRB Wisconsin experiment from October 12 through November 2, *NASA Tech. Mem. 102596*, 272 pp., 1990b.

Whitlock, C. H., S. K. Cox, and S. R. LeCroy, Downwelled longwave surface irradiance data from five sites for the FIRE/SRB Wisconsin experiment from October 12 through November 2, *NASA Tech. Mem. 102597*, 187 pp, 1990c.

Wick, G. A., W. J. Emery, and P. Schluessel, A comprehensive comparison between satellite-measured skin and multichannel sea surface temperature, *J. Geophys. Res., 97*, 5569-5595, 1992.

Wielicki, B. A., and R. N. Green, Cloud identification for ERBE radiative flux retrieval, *J. Appl. Meteorol., 28*, 1133-1146, 1989.

Wittmeyer, I. L., and T. H. Vonder Haar, Analysis of the global ISCCP TOVS water vapor climatology, *J. Clim., 7*, 325-333, 1994.

Young, G. S., D. V. Ledvina, and C. W. Fairall, Influence of precipitating convection on the surface energy budget observed during a Tropical Ocean Global Atmosphere pilot cruise in the tropical western Pacific Ocean, *J. Geophys. Res., 97*, 9595-9603, 1992.

Zhang, Y.-C., W. B. Rossow, and A. A. Lacis, Calculation of surface and top of atmosphere radiative fluxes from physical quantities based on ISCCP data sets, 1, Method and sensitivity to input data uncertainties, *J. Geophys. Res.*, this issue.

W. B. Rossow, NASA Goddard Institute for Space Studies, 2880 Broadway, New York, NY 10025.

Y.-C. Zhang, NASA Goddard Institute for Space Studies, Columbia University, 2880 Broadway, New York, NY 10025.

(Received April 21, 1994; revised October 7, 1994; accepted October 10, 1994.)